Statistical properties of shear and nonshear velocity components in isotropic turbulence and turbulent jets

Ryo Enoki

Department of Aerospace Engineering, Nagoya University, Nagoya 464-8603, Japan

Tomoaki Watanabe ⊕*

Education and Research Center for Flight Engineering, Nagoya University, Nagoya 464-8603, Japan

Koji Nagata ⊕

Department of Mechanical Engineering and Science, Kyoto University, Kyoto 615-8530, Japan

The triple decomposition of a velocity gradient tensor, which extracts local fluid motions of shear, rigid-body rotation, and irrotational strain, is extended to the decomposition of velocity vectors into shear and nonshear components. The present approach adapts the Biot-Savart law to reconstruct shear and nonshear velocities from the vorticity vectors of shear and rigid-body rotation, respectively. These velocities are related to the flows induced by small-scale shear layers or vortex tubes. The decomposed velocities are investigated with direct numerical simulations of isotropic turbulence and temporally evolving planar jets. The r.m.s. values of shear and nonshear velocities are about 70% and 30% of the r.m.s. value of total velocity fluctuations, and shear layers have a greater contribution to velocity fluctuations than vortex tubes. The shear and nonshear velocities are positively correlated at large scales, and the momentum transfer due to their interaction actively occurs at scales greater than 20 times the Kolmogorov scale. The contributions of shear and nonshear velocities to the Reynolds stress hardly depend on flows. The energy spectra of these velocities collapse well at small scales under Kolmogorov normalization. The present analysis of the turbulent jet confirms that shearing motion has dominant contributions to the production and diffusion of turbulent kinetic energy and the turbulent transport of a passive scalar. In addition, the energy transfer across scales is shown to be dominated by the large-scale velocity gradients arising from shearing motion and the small-scale stresses due to the shear velocity and its interaction with the nonshear component.

I. INTRODUCTION

Turbulence is an important phenomenon in various scientific problems and engineering applications. It is characterized by fluid motions with a wide range of scales. Velocity fluctuations associated with large-scale motions efficiently transport momentum, heat, and chemical substances [1]. Small-scale motions are strongly influenced by viscous effects, by which kinetic energy is dissipated. In addition, the rates of heat conduction and molecular diffusion are also enhanced by small-scale turbulent motions. The small-scale properties of turbulence are studied with a velocity gradient tensor ∇u [2]. Hereafter, components of tensors and vectors are denoted with

---

*Author to whom correspondence should be addressed: watanabe.tomoaki@c.nagoya-u.jp

subscripts, e.g., $(\nabla \boldsymbol{u})_{ij} = \partial u_i / \partial x_j$. The analyses of $\nabla \boldsymbol{u}$ often adapt the decomposition into symmetric and antisymmetric components as $(\nabla \boldsymbol{u})_{ij} = S_{ij} + \Omega_{ij}$, where $S_{ij} = [(\nabla \boldsymbol{u})_{ij} + (\nabla \boldsymbol{u})_{ji}]/2$ and $\Omega_{ij} = [(\nabla \boldsymbol{u})_{ij} - (\nabla \boldsymbol{u})_{ji}]/2$ are the rate-of-strain tensor and rate-of-rotation tensor, respectively [3]. The kinetic energy dissipation rate is defined as $2\nu S_{ij} S_{ij}$ with kinematic viscosity ν, while vortical structures are often identified with enstrophy $\omega^2/2 = \Omega_{ij}\Omega_{ij}$. This decomposition has been extensively utilized in the investigation of turbulence [3].

Recent studies have indicated the importance of a shear contribution to the velocity gradient tensor. Vortex identification schemes based on enstrophy cannot distinguish tubular and sheetlike structures with large enstrophy [4]. The former structures are known as vortex tubes, where rotation described by Ω_{ij} is more significant than deformation S_{ij}. The latter structures are called vortex sheets, where both rotation and deformation are significant. The vortex sheets are characterized by shearing motion, which contributes to both Ω_{ij} and S_{ij} [5], and they are also called shear layers in recent studies [6]. Therefore, recent vortex identification schemes consider the extraction of shearing motion from the velocity gradient tensor. This approach is adapted by the triple decomposition and the Rortex-based decomposition [7,8], which have proved useful in analyzing local flow topology and related flow structures. The triple decomposition considers three local fluid motions of shear (S), rigid-body rotation (R), and elongation (E) (irrotational strain), as $\nabla \boldsymbol{u} = \nabla \boldsymbol{u}_S + \nabla \boldsymbol{u}_R + \nabla \boldsymbol{u}_E$. The components of shear and rigid-body rotation are useful to investigate shear layers and vortex tubes, respectively, as proved in early studies of the triple decomposition [9,10]. The advantage of the triple decomposition is in the extraction of the shear component of the velocity gradient tensor. In the classical double decomposition, $\nabla \boldsymbol{u}$ is split into S_{ij} and Ω_{ij}. Because shearing motion contributes to both S_{ij} and Ω_{ij}, these tensors of the double decomposition cannot directly distinguish shearing motion from other motions. Due to the capability of the triple decomposition in distinguishing shear and rigid-body rotation, it has been used in detecting turbulent structures associated with them. As reviewed below, this feature of the triple decomposition has helped us understand the important properties of local shearing motion.

The triple decomposition has proved its effectiveness in studying local turbulent motions in previous studies. Eisma *et al.* [10] adapted the triple decomposition in a two-dimensional form to experimental datasets of a turbulent boundary layer obtained with two-dimensional and two-component particle image velocimetry. They successfully identified thin shear layers with the vorticity defined for the shear component $\nabla \boldsymbol{u}_S$. They observed a large velocity jump across the shear layers. The triple decomposition for a three-dimensional velocity gradient tensor in turbulence was also reported for isotropic turbulence, where the computational cost of the decomposition algorithm was shown to be reasonable enough for a direct numerical simulation (DNS) database of three-dimensional turbulent flows [11]. Later, the triple decomposition has been applied to three-dimensional velocity profiles of various turbulent flows. Small-scale shear layers detected with the norm of $\nabla \boldsymbol{u}_S$ were investigated in isotropic turbulence [12]. A conditional sampling technique for the shear layers calculates the statistics in a three-dimensional local coordinate system, called a shear coordinate, with the origin located at the center of the shear layers. The orientation of the shear coordinate was determined with the components of $\nabla \boldsymbol{u}_S$. The shear layers were shown to form in a biaxial strain field with an extensive strain in the shear vorticity direction and a compressive strain in the layer-normal direction, where the interaction between the shear and biaxial strain causes enstrophy production and strain self-amplification. The components of mean velocity vectors associated with the shear and biaxial strain exhibit a distinct jump within the shear layers. Fiscaletti *et al.* [13] investigated the shear layers with experiments of turbulent jets [14] and DNS of a turbulent mixing layer [15]. They also observed a mean velocity jump near the shear layers. These studies have shown that the length and velocity scales of shear layers are characterized by Kolmogorov scales. The mean velocity profile around the shear layers is related to the mean flow pattern observed in the reference frame defined with the eigenvectors of the rate-of-strain tensor [16–18], which successfully explains various statistical properties of turbulence [19,20]. The shear layer characteristics evaluated with the triple decomposition were also used in the stability analysis

of small-scale shear layers [21], which confirmed that the perturbation response of shear layers can be important for controlling small-scale turbulence with external disturbance.

The application of the triple decomposition to turbulence is restricted to the studies of small-scale properties, most of which concern small-scale shear layers discussed above. This is because the velocity gradient describes local flow topology around one point in a flow, which is useful to define small-scale turbulent structures. However, their relevance to large-scale phenomena is not clear so far. Large-scale properties are important because large-scale turbulent motions possess a large part of kinetic energy. Therefore, flow evolutions are often governed by large-scale properties of the flow. For example, the order of the kinetic energy dissipation rate is imposed by the length and velocity scales of large-scale motions [22]. In addition, turbulent transports are also dominated by large-scale velocity fluctuations, as confirmed by Fourier analyses of turbulent fluxes of momentum and scalars such as mass fractions and temperature [23–25]. Because the triple decomposition considers only three types of local fluid motion described by the velocity gradient tensor, the role of these motions in the phenomena dominated by large scales is difficult to assess with the triple decomposition.

In incompressible flows, a velocity field $\boldsymbol{u}$ is related to a velocity gradient tensor by the Biot-Savart law, which is written with a vorticity vector $\boldsymbol{\omega} = \nabla \times \boldsymbol{u}$ as $\boldsymbol{u} = -\nabla \times (\nabla^{-2} \boldsymbol{\omega})$. For a given vorticity field, this relation can be used to reconstruct the velocity field under appropriate boundary conditions. This procedure is often used in decompositions of flows based on the vorticity vector. One of the examples is the extraction of coherent structures with an orthogonal wavelet transform [26]. The vorticity vector is decomposed into coherent and incoherent components with the wavelet transform, while the corresponding components of the velocity vector are obtained with the Biot-Savart law [27,28]. This reconstruction of the velocity vectors from the decomposed vorticity vectors has been adapted for the analyses of turbulent transport phenomena, such as turbulent mixing [29] and entrainment in turbulent free shear flows [30].

The present study proposes the reconstruction of the velocity fields from the vorticity vectors decomposed by the triple decomposition. The previous studies of the triple decomposition have considered only local fluid motion described by the velocity gradient tensor. Even though the velocity gradient tensor is defined locally at one point, its influence on the flow is not local as also observed for the relation between the vorticity and velocity fields. The present approach enables us to study the influence of the local fluid motions described by the triple decomposition on an entire flow field. The vorticity vector can be uniquely decomposed into two components of shear and rigid-body rotation with the triple decomposition. The Biot-Savart law is applied to these decomposed vorticity vectors. This approach is motivated by two types of small-scale turbulent structures, namely, vortex tubes characterized by rigid-body rotation and small-scale shear layers characterized by shearing motion. Both structures play important roles in various phenomena related to turbulence, such as particle transport [31], entrainment in intermittent turbulent flows [32,33], and enstrophy production and strain self-amplification [12]. Although a flow field around a single isolated structure can be studied with idealized models [3], the interaction of many vortex tubes and shear layers result in a complicated velocity profile in turbulent flows. The velocity vectors reconstructed by the decomposed vorticity vectors of the triple decomposition are related to the flow fields arising from the superposition of the flows induced by many shear layers or vortex tubes. Therefore, the present velocity decomposition is expected to provide additional insights into these small-scale turbulent structures, especially their roles in large-scale phenomena.

The triple decomposition extended to velocity as the velocity decomposition into shear and nonshear components is tested with direct numerical simulations (DNS) of homogeneous isotropic turbulence and planar jets. The present study confirms that these velocity components have universal statistical properties that hardly differ for isotropic turbulence and planar jets with a wide range of Reynolds numbers. We also present the application of the proposed decomposition to the analyses of a kinetic energy budget and scalar mixing in turbulent flows, which will be useful in understanding the role of the three local fluid motions of the triple decomposition in various turbulent transport phenomena. The present results provide evidence that shearing motion, related to small-scale shear layers investigated in early studies of the triple decomposition, is essential in the turbulent transport.

The paper is organized as follows. Section II presents the decomposition of a velocity vector with the triple decomposition. DNS databases of homogeneous isotropic turbulence and planar jets are described in Sec. III. Section IV discusses the properties of the decomposed velocity vectors in these turbulent flows. Finally, the paper is summarized in Sec. V.

II. DECOMPOSITION OF A VELOCITY FIELD BASED ON THE TRIPLE DECOMPOSITION

A. The triple decomposition of a velocity gradient tensor

The triple decomposition considers three local fluid motions: shear, rigid-body rotation, and irrotational strain called elongation [7]. An incompressible fluid is considered throughout the paper. The velocity gradient tensor is decomposed as $\nabla \boldsymbol{u} = \nabla \boldsymbol{u}_S + \nabla \boldsymbol{u}_R + \nabla \boldsymbol{u}_E$, which is locally defined at a given position $\boldsymbol{x}$. The decomposition has to be applied in a so-called basic reference frame (BRF), where the decomposition formula fully extracts the shear component from $\nabla \boldsymbol{u}$. Several implementations of the triple decomposition of three-dimensional flows have been proposed in previous studies [11,34]. The present study follows the original algorithm, which was also used for three-dimensional turbulent flows [7,11]. A coordinate transformation matrix $\boldsymbol{Q}(\theta_1, \theta_2, \theta_3)$ for three successive rotations about different axes is introduced to identify the BRF:

$$\boldsymbol{Q} = \begin{pmatrix} \cos\theta_1 \cos\theta_2 \cos\theta_3 - \sin\theta_1 \sin\theta_3 & \sin\theta_1 \cos\theta_2 \cos\theta_3 + \cos\theta_1 \sin\theta_3 & -\sin\theta_2 \cos\theta_3 \\ -\cos\theta_1 \cos\theta_2 \sin\theta_3 - \sin\theta_1 \cos\theta_3 & -\sin\theta_1 \cos\theta_2 \sin\theta_3 + \cos\theta_1 \cos\theta_3 & \sin\theta_2 \sin\theta_3 \\ \cos\theta_1 \sin\theta_2 & \sin\theta_1 \sin\theta_2 & \cos\theta_2 \end{pmatrix} \tag{1}$$

with angles $(\theta_1, \theta_2, \theta_3)$ in the ranges of $0° \leqslant \theta_1 \leqslant 180°$, $0° \leqslant \theta_2 \leqslant 180°$, and $0° \leqslant \theta_3 \leqslant 90°$. The rotated reference frame $\boldsymbol{x}^*$ is obtained by applying $\boldsymbol{Q}$ to an original reference frame $\boldsymbol{x}$ of numerical simulations or laboratory experiments. Hereafter, the asterisk superscript represents a variable evaluated in the rotated reference frame. The velocity gradient tensor in $\boldsymbol{x}^*$ is calculated as $(\nabla \boldsymbol{u})^* = \boldsymbol{Q}(\nabla \boldsymbol{u})\boldsymbol{Q}^T$. The BRF assumes that a variable called an interaction scalar, $I^* = |\Omega_{12}^* S_{12}^*| + |\Omega_{23}^* S_{23}^*| + |\Omega_{31}^* S_{31}^*|$, becomes the largest among all the possible reference frames. The BRF can be determined by examining I^* in rotated reference frames with many sets of $(\theta_1, \theta_2, \theta_3)$. Specifically, $(\theta_1, \theta_2, \theta_3)$ are discretely changed with an increment of $5°$, and I^* is calculated for each reference frame. The increment of $5°$ was shown to be small enough to accurately determine the BRF [11,13]. Then $(\theta_1, \theta_2, \theta_3)$ which yields the largest I^* can be used to define the BRF. Once the BRF is identified, the following decomposition is applied to $\nabla \boldsymbol{u}^*$ in the BRF:

$$(\nabla \boldsymbol{u}_{RES})^*_{ij} = \text{sgn}[(\nabla \boldsymbol{u})^*_{ij}] \min[|(\nabla \boldsymbol{u})^*_{ij}|, |(\nabla \boldsymbol{u})^*_{ji}|], \tag{2}$$

$$(\nabla \boldsymbol{u}_S)^*_{ij} = (\nabla \boldsymbol{u})^*_{ij} - (\nabla \boldsymbol{u}_{RES})^*_{ij}, \tag{3}$$

with $i, j = 1, 2$, and 3. Here $\nabla \boldsymbol{u}_{RES}$ is called a residual tensor and does not contain shearing motion, while the shear is represented by $\nabla \boldsymbol{u}_S$. In addition, the conventional decomposition into symmetric and antisymmetric parts applied to $\nabla \boldsymbol{u}_{RES}$ yields the components of elongation and rigid-body rotation as

$$(\nabla \boldsymbol{u}_E)^*_{ij} = \tfrac{1}{2}(\nabla \boldsymbol{u}_{RES})^*_{ij} + \tfrac{1}{2}(\nabla \boldsymbol{u}_{RES})^*_{ji}, \tag{4}$$

$$(\nabla \boldsymbol{u}_R)^*_{ij} = \tfrac{1}{2}(\nabla \boldsymbol{u}_{RES})^*_{ij} - \tfrac{1}{2}(\nabla \boldsymbol{u}_{RES})^*_{ji}. \tag{5}$$

Finally, these tensors in the original reference frame, $\nabla \boldsymbol{u}_S$, $\nabla \boldsymbol{u}_R$, and $\nabla \boldsymbol{u}_E$, are obtained by applying the inverse transformation of $\boldsymbol{Q}$ to $(\nabla \boldsymbol{u}_S)^*$, $(\nabla \boldsymbol{u}_R)^*$, and $(\nabla \boldsymbol{u}_E)^*$, respectively.

B. Reconstruction of shear and nonshear velocity fields

The original triple decomposition is applied to the velocity gradient tensor, which expresses local fluid motion at one point in a flow. The present study further extends the triple decomposition to the

decomposition of a velocity field. In the triple decomposition, a vorticity vector $\boldsymbol{\omega}$ is decomposed into the shear (S) and nonshear (NS) components as $\boldsymbol{\omega} = \boldsymbol{\omega}_S + \boldsymbol{\omega}_{NS}$ with $\omega_{S_i} = \epsilon_{ijk}(\nabla \boldsymbol{u}_S)_{jk}$ and $\omega_{NS_i} = \epsilon_{ijk}(\nabla \boldsymbol{u}_{RES})_{jk}$, where ϵ_{ijk} is the Levi-Civita symbol. The nonshear vorticity is associated with rigid-body rotation $\nabla \boldsymbol{u}_R$ because elongation $\nabla \boldsymbol{u}_E$ does not contribute to the vorticity. The trace of $\nabla \boldsymbol{u}_S$ and $\nabla \boldsymbol{u}_{RES}$ is zero because of incompressibility, and therefore, the present study considers the reconstruction of the velocity fields corresponding to these vorticity vectors with the Biot-Savart law $\boldsymbol{u} = -\nabla \times (\nabla^{-2}\boldsymbol{\omega})$. With vector potentials $\boldsymbol{\varphi} = (\varphi_1, \varphi_2, \varphi_3)$ defined as $\nabla^2 \boldsymbol{\varphi} = \boldsymbol{\omega}$, the velocity vector is expressed as $\boldsymbol{u} = -\nabla \times \boldsymbol{\varphi}$, which can also be written as $u_i = -\nabla \times \varphi_i$ with $\nabla^2 \varphi_i = \omega_i$ for $i = 1, 2$, and 3. Similarly, the vector potentials defined with $\nabla^2 \boldsymbol{\varphi}_S = \boldsymbol{\omega}_S$ and $\nabla^2 \boldsymbol{\varphi}_{NS} = \boldsymbol{\omega}_{NS}$ are related to the shear and nonshear components of the velocity vector, $\boldsymbol{u}_S$ and $\boldsymbol{u}_{NS}$, respectively. Although the Biot-Savart law for the original solenoidal velocity vector, $\boldsymbol{u} = -\nabla \times (\nabla^{-2}\boldsymbol{\omega})$, relates $\boldsymbol{u}$ to the rate-of-rotation tensor Ω_{ij}, it does not provide an explicit relation between $\boldsymbol{u}$ and the rate-of-strain tensor S_{ij}. However, the symmetric part of $\nabla \boldsymbol{u}$ still provides S_{ij} even if $\boldsymbol{u}$ is calculated from the vorticity vector with the Biot-Savart law. For the same reason, $\nabla \boldsymbol{u}_E$ and $\nabla \boldsymbol{u}_R$ are the symmetric and antisymmetric parts of the gradient tensor of $\boldsymbol{u}_{NS}$, respectively, although $\boldsymbol{u}_{NS}$ is calculated from $\boldsymbol{\omega}_{NS}$, which is written with the components of $\nabla \boldsymbol{u}_R$. Because of this relation between $\boldsymbol{u}_{NS}$ and $\nabla \boldsymbol{u}_E$, $\boldsymbol{u}_{NS}$ is called nonshear velocity instead of the velocity of rigid-body rotation.

The detailed numerical procedure to reconstruct the shear and nonshear velocity components is provided here. The present study solves the Poisson equations to obtain the vector potentials for the shear component, $\boldsymbol{\varphi}_S$, which yield $\boldsymbol{u}_S$, while the nonshear component $\boldsymbol{u}_{NS}$ is calculated by subtracting $\boldsymbol{u}_S$ from the total velocity vector. Generally, the velocity vector $\boldsymbol{u}$ can be decomposed as

$$\boldsymbol{u} = \langle \boldsymbol{u} \rangle + \boldsymbol{u}_S + \boldsymbol{u}_{NS}, \tag{6}$$

where $\langle \boldsymbol{u} \rangle$ is the mean velocity vector. First, the triple decomposition is applied to an instantaneous three-dimensional profile of $\nabla \boldsymbol{u}$ to obtain $\nabla \boldsymbol{u}_S$, from which $\boldsymbol{\omega}_S = (\omega_{S_1}, \omega_{S_2}, \omega_{S_3})$ is calculated as $\omega_{S_i} = \epsilon_{ijk}(\nabla \boldsymbol{u}_S)_{jk}$. Then the vector potentials $\boldsymbol{\varphi}_S = (\varphi_{S_1}, \varphi_{S_2}, \varphi_{S_3})$ are calculated by solving the Poisson equations, $\nabla^2 \varphi_{S_i} = \omega_{S_i}$ for $i = 1, 2$, and 3. Although a velocity vector can be obtained from $\boldsymbol{\varphi}_S$ as $\tilde{\boldsymbol{u}}_S = -\nabla \times \boldsymbol{\varphi}_S$, $\tilde{\boldsymbol{u}}_S$ often partially contains the contribution of a mean flow while Eq. (6) assumes that the mean flow is separated by $\langle \boldsymbol{u} \rangle$ and the averages of $\boldsymbol{u}_S$ and $\boldsymbol{u}_{NS}$ are zero. Therefore, the average of $\tilde{\boldsymbol{u}}_S$ is subtracted to obtain $\boldsymbol{u}_S$ as $\boldsymbol{u}_S = \tilde{\boldsymbol{u}}_S - \langle \tilde{\boldsymbol{u}}_S \rangle$. Finally, the nonshear component is calculated as $\boldsymbol{u}_{NS} = \boldsymbol{u} - \langle \boldsymbol{u} \rangle - \boldsymbol{u}_S$. The present decomposition does not assume the orthogonality of $\boldsymbol{u}_S$ and $\boldsymbol{u}_{NS}$, whose correlation is not generally zero. The correlation between $\boldsymbol{u}_S$ and $\boldsymbol{u}_{NS}$ represents the momentum transport due to the interaction of shearing and other motions of the triple decomposition.

An early study of shear layers and vortex tubes also adapted the Biot-Savart law to obtain the velocity related to these structures [35]. The Biot-Savart law was applied to a truncated vorticity field, for which the vorticity vector is set to zero in regions where the structures of interest do not appear. This approach does not decompose the vorticity vector itself, unlike the triple decomposition. The analysis of shear layers has confirmed that because vortex tubes often appear within shear layers, they can share the same region in a flow [36]. Therefore, the velocity profile obtained from the truncated vorticity for shear layers or vortex tubes is contaminated by the other structures. This problem does not exist for the triple decomposition because the vorticity vector is decomposed into the components of shear layers and vortex tubes before the velocity field is reconstructed. This feature enables us to define the interaction between shear and nonshear velocities, as explained below.

III. DNS DATABASES OF HOMOGENEOUS ISOTROPIC TURBULENCE AND TEMPORALLY EVOLVING PLANAR JETS

The triple decomposition extended to a velocity field is tested with DNS databases of homogeneous isotropic turbulence and temporally evolving planar jets. The same databases were used in

TABLE I. DNS databases of homogeneous isotropic turbulence (HIT) and temporally evolving planar jets (JET).

Case	HIT1	HIT2	HIT3	HIT4	JET1	JET2
N_x	256	512	1024	2048	432	864
N_y	256	512	1024	2048	600	1200
N_z	256	512	1024	2048	288	576
Re_J	–	–	–	–	4000	10 000
Re_λ	43	72	128	202	59	97

our previous studies [6,12,36]. Both flows are simulated with an in-house DNS code based on the fractional step method, which solves incompressible Navier-Stokes equations written as

$$\frac{\partial u_j}{\partial x_j} = 0, \tag{7}$$

$$\frac{\partial u_i}{\partial t} + \frac{\partial u_i u_j}{\partial x_j} = -\frac{1}{\rho}\frac{\partial p}{\partial x_i} + \nu\frac{\partial^2 u_i}{\partial x_j \partial x_j}, \tag{8}$$

Here x_i is the position in the i direction, t is time, p is the pressure, ρ is the constant density of the fluid, and ν is the kinematic viscosity. The velocity components in the x, y, and z directions are respectively denoted by u, v, and w. For temporally evolving planar jets, the transport equation for passive scalar φ is also solved along with the Navier-Stokes equations:

$$\frac{\partial \phi}{\partial t} + \frac{\partial \phi u_j}{\partial x_j} = D\frac{\partial^2 \phi}{\partial x_j \partial x_j}, \tag{9}$$

where D is the diffusivity coefficient. Fully conservative central difference schemes with fourth-order and second-order accuracies are applied to homogeneous and inhomogeneous directions, respectively [37]. A three-stage and third-order low-storage Runge-Kutta scheme is adapted for time integration. The biconjugate gradient stabilized method is employed to solve the Poisson equation for pressure. The DNS code has been validated by comparing the results with other experiments and numerical simulations [6,38–40]. The DNS databases are briefly described below.

The shear and nonshear components of velocity vectors are statistically analyzed for isotropic turbulence and temporally evolving planar jets. An average of a flow variable f is denoted by $\langle f \rangle$ while the fluctuations are defined as $f' = f - \langle f \rangle$. The averages are taken as volume averages in a domain and ensemble averages of different snapshots for the isotropic turbulence. For the temporally evolving planar jets, spatial averages in statistically homogeneous directions are used together with ensemble averages of different simulations.

A. Homogeneous isotropic turbulence

Statistically steady homogeneous isotropic turbulence is investigated with the DNS databases [12,36]. Periodic boundary conditions are applied in three directions. The flow is sustained at a statistically steady state with a linear forcing scheme [41]. The cubic computational domain has a size of $L^3 = (5.3L_I)^3$, where L_I is the length scale of large-scale turbulent motions determined by the forcing scheme. Four cases with different Reynolds numbers are considered in this study as summarized in Table I, where (N_x, N_y, N_z) are the numbers of grid points in the three directions and $Re_\lambda = u_{rms}\lambda/\nu$ is the turbulent Reynolds number. Here the r.m.s. value of velocity fluctuations is $u_{rms} = \sqrt{(\langle u^2 \rangle + \langle v^2 \rangle + \langle w^2 \rangle)/3}$, the averaged kinetic energy dissipation rate is $\varepsilon = \langle 2\nu S_{ij}S_{ij} \rangle$, and the Taylor microscale is $\lambda = (15u_{rms}^2 \nu/\varepsilon)^{1/2}$. The spatial resolution Δ is the same in the three directions, and Δ divided by the Kolmogorov scale $\eta = (\nu^3/\varepsilon)^{1/4}$ is about 0.8 for all simulations. The numbers of snapshots used for ensemble averages are 8, 8, 6, and 2 for HIT1, HIT2, HIT3,

and HIT4, respectively. The Poisson equations for the vector potentials of shear velocity are solved in wave number space with a fast Fourier transform, and the shear and nonshear velocities are calculated as explained in Sec. II.

B. Temporally evolving turbulent planar jets

The DNS databases of temporally evolving turbulent planar jets in our previous papers [6,42] are used in this study. The simulations of temporally evolving shear flows use periodic boundary conditions in the streamwise direction, in which the flows are statistically homogeneous. Then the turbulent flow develops with time rather than with a streamwise position. This methodology of temporal simulations has been adapted for various canonical turbulent shear flows, such as jets [43–46], wakes [47], mixing layers [48], boundary layers [49,50], and grid turbulence [38,51]. These studies have confirmed that the transverse profiles of various statistics of velocity fluctuations hardly differ between temporally and spatially evolving turbulent flows.

The temporally evolving planar jet is statistically homogeneous in the streamwise (x) and spanwise (z) directions and develops in the transverse (y) direction with time. The statistics can be evaluated with averages $\langle f \rangle$ taken on x-z planes as functions of y and t. The initial profile of the mean streamwise velocity is given by $\langle u \rangle = U_J/2 + (U_J/2)\tanh[(H - 2|y|)/4\theta_J]$, where U_J and H are the initial velocity and width of the jet, respectively. The jet center is at $y = 0$. In addition, the scalar transport equation, Eq. (9), is solved with the initial profile of ϕ given by $\phi = \phi_J/2 + (\phi_J/2)\tanh[(H - 2|y|)/4\theta_J]$, for which ϕ/ϕ_J is 1 and 0 inside and outside the jet, respectively. In addition, spatially correlated random noise is superimposed onto the mean velocity [52]. Periodic boundary conditions are applied in the x and z directions while free-slip boundary conditions are applied in the y direction. The size of the computational domain is $(L_x, L_y, L_z) = (6H, 10H, 4H)$. It was confirmed that a velocity autocorrelation function in the present DNS agrees well with other DNS and experiments of spatially evolving jets [53,54], suggesting that the domain size is large enough to reproduce the large-scale characteristics of the planar jet [39]. The jet Reynolds number is defined as $\mathrm{Re}_J = U_J H/\nu$. Table I also presents the parameters of the DNS databases of the planar jets. Two cases are simulated with $\mathrm{Re}_J = 4000$ and $100\,000$. The thickness of the initial shear layers at the edges of the jet is $\theta_J = 0.01H$. The Schmidt number is $\mathrm{Sc} = \nu/D = 1$. The computational grid is uniformly spaced in the x and z directions while nonuniform grid spacing is employed in the y direction, for which the grid spacing becomes smaller toward the jet center. From the initial laminar state at $t = 0$, the turbulent jet develops with time. The fully developed turbulent regime at $t = 20(H/U_J)$ is analyzed in this study. The velocity statistics at this time have been presented in our previous papers [6,42], where the DNS results are compared with other experimental and numerical data. The grid sizes are 1.5η in the x and z directions and about 1.1η in the y direction inside the jet. The values of the turbulent Reynolds number Re_λ at $y = 0$ are 59 for $\mathrm{Re}_J = 4000$ and 97 for $\mathrm{Re}_J = 10\,000$. For the planar jets, the biconjugate gradient stabilized method is used to solve the Poisson equations to calculate the vector potentials of shear velocity.

IV. RESULTS AND DISCUSSION

A. Visualization of shear and nonshear velocity components

Figure 1 visualizes the y-directional components of shear and nonshear velocity vectors, v_S and v_{NS}, on a y-z plane in HIT4. Both velocity components contain fluctuations with a wide range of scales. The ranges of the color contours suggest that shearing motion has a larger contribution to velocity fluctuations than other motions because $|v_S|$ tends to be larger than $|v_{NS}|$. Large-scale distributions of v_S and v_{NS} are positively correlated: regions with $v_S > 0$ tend to have $v_{NS} > 0$, while the opposite trend is found for $v_S < 0$ and $v_{NS} < 0$. Therefore, momentum in one motion of the triple decomposition is transferred by other motions at large scales. This is further discussed with the normal component of the Reynolds stress below. However, small-scale distributions are different for shear and nonshear velocity components. As shown in a box in Fig. 1(b), small circular
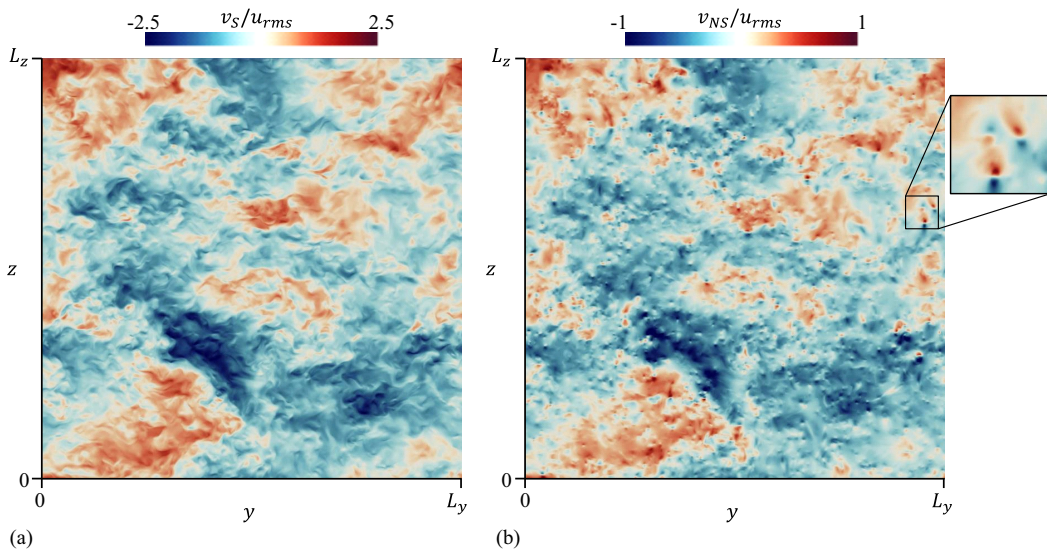
FIG. 1. Two-dimensional profiles of (a) shear and (b) nonshear components of y-directional velocity on a y-z plane in HIT4.

spots with large positive and negative values appear next to each other in the profile of v_{NS}. These patterns are related to small-scale vortex tubes with the axis perpendicular to the visualized plane, as also shown below. On the other hand, the shear component does not have similar patterns at small scales.

The correlation between the shear and nonshear velocities at large scales is possibly related to the spatial distribution of small-scale turbulent structures explained here. The shear layers and vortex tubes are known to form their clusters. The shear layers often cause intense kinetic energy dissipation due to the large velocity gradient of shearing motion. The clusters of flow regions with intense dissipation mostly overlap those of large enstrophy, which are partially related to vortex tubes [55]. Consistently, visualization of shear layers and vortex tubes identified with the triple decomposition has shown that their clusters occupy the same flow regions [36]. The correspondence of the cluster locations of shear layers and vortex tubes is explained with their local spatial organization because the shear layers often appear in the vicinity of vortex tubes [17,36]. These studies have also shown that the orientation of the shear layers and nearby vortex tubes are strongly correlated.

Figure 2 shows the vectors of shear and nonshear velocities with color contours of the intensities of shear and rigid-body rotation in HIT4. The intensities of shear and rigid-body rotation are defined as $I_S = \sqrt{2(\nabla \boldsymbol{u}_S)_{ij}(\nabla \boldsymbol{u}_S)_{ij}}$ and $I_R = \sqrt{2(\nabla \boldsymbol{u}_R)_{ij}(\nabla \boldsymbol{u}_R)_{ij}}$, respectively [42]. A small part of the computational domain is shown for visualizing small-scale turbulent structures. Previous studies of the triple decomposition have shown that small-scale shear layers (vortex sheets) and vortex tubes have large values of I_S and I_R, respectively [11]. In Fig. 2(a) a shear layer is visualized as a thin layer with large I_S, and the vectors of $\boldsymbol{u}_S$ successfully detect flows toward the bottom left and top right on the left and right of the shear layer, respectively. These parallel flows in opposite directions contribute to shearing motion in the layer. In Fig. 2(b) circular regions with large I_R visualize slices of vortex tubes. Around the vortex tubes, rotating motion is identified in the velocity vectors of $\boldsymbol{u}_{NS}$. Therefore, the velocity components associated with shear layers and vortex tubes are well extracted by the present method. These clear relations of shear and nonshear velocities to the shear layer and vortex tube are easily observed when these structures are isolated, as shown in Fig. 2. The original triple decomposition is useful to study local fluid motion of each turbulent structure. For the present DNS of isotropic turbulence, the numbers of vortex tubes and shear layers
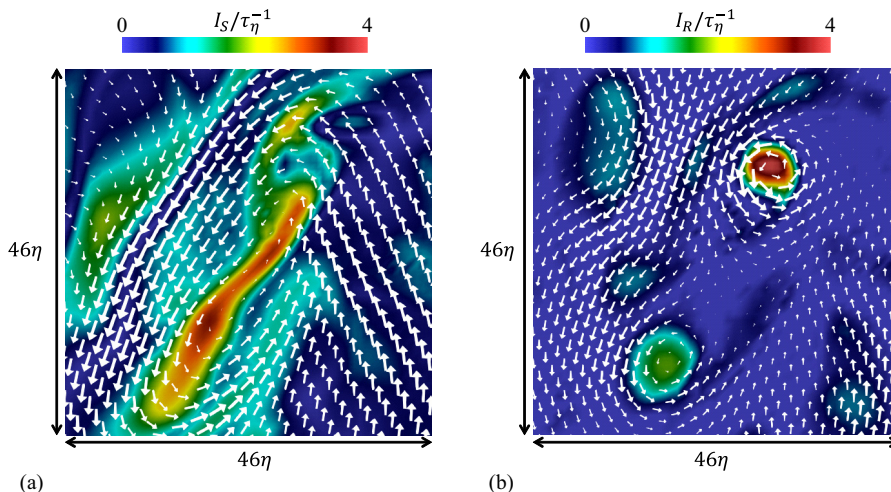
FIG. 2. Two-dimensional profiles of (a) shear and (b) nonshear components of velocity vectors on a y-z plane in HIT4. The color contours visualize the intensities of shear I_S and rigid-body rotation I_R in panels (a) and (b), respectively. The Kolmogorov timescale $\tau_\eta = (\nu/\varepsilon)^{1/2}$ is used to normalize I_S and I_R. The length of the arrows indicates the vector magnitude. Only a small part of the domain is shown.

were evaluated by detecting them by applying thresholds to I_S and I_R [21]. The numbers exceed 10^4 depending on the Reynolds numbers. The threshold-dependence test has shown that although the number of the detected structures is sensitive to the thresholds, the order estimate is not influenced by a particular threshold choice. The superposition of the flows induced by many structures results in a complicated velocity distribution in Fig. 1. A flow induced by each of the structures has been studied extensively [42,56]. However, the velocity distribution arising from many shear layers or vortex tubes is less understood because of the difficulty in reconstructing the flow induced by many shear layers or vortex tubes. The kinetic energy of velocity fluctuations is possessed mainly by large-scale turbulent motion. Although $\boldsymbol{u}_S$ and $\boldsymbol{u}_{NS}$ locally exhibit patterns related to shear layers and vortex tubes at small scales, respectively, many of these structures also cause large-scale velocity fluctuations, as described by the Biot-Savart law that relates a velocity field to the spatial integral of the vorticity vector.

Figure 3 visualizes three components of $\boldsymbol{u}_S$ and $\boldsymbol{u}_{NS}$ in JET2. The jet is visualized on an x-y plane at $t = 20(H/U_J)$, which is in a fully developed state. The turbulent jet is located for $|y/H| \lesssim 1.0$–1.5. The velocity profiles are different between the turbulent jet and the ambient (laminar) fluid. As also found for isotropic turbulence, velocity fluctuations with a wide range of scales are observed in the jet for all the velocity components. Pairs of small circular regions with positive and negative values of u_{NS} are also found in the jet, as shown in the boxes in Fig. 3(d). As also found for isotropic turbulence, the positive correlation in the large-scale distribution is found for each component of $\boldsymbol{u}_S$ and $\boldsymbol{u}_{NS}$ in the turbulent jet. Therefore, the momentum transfer by the interaction of shear and other motions occurs even in inhomogeneous turbulence.

B. Statistical properties of shear and nonshear velocity components

The statistical properties of shear and nonshear velocity components are examined for the isotropic turbulence and planar jets with different Reynolds numbers. The Reynolds stress is defined as $\langle u'_i u'_j \rangle$, which can be decomposed with Eq. (6) as

$$\langle u'_i u'_j \rangle = \langle u_{S_i} u_{S_j} \rangle + \langle u_{NS_i} u_{NS_j} \rangle + \langle u_{S_i} u_{NS_j} \rangle + \langle u_{NS_i} u_{S_j} \rangle, \tag{10}$$
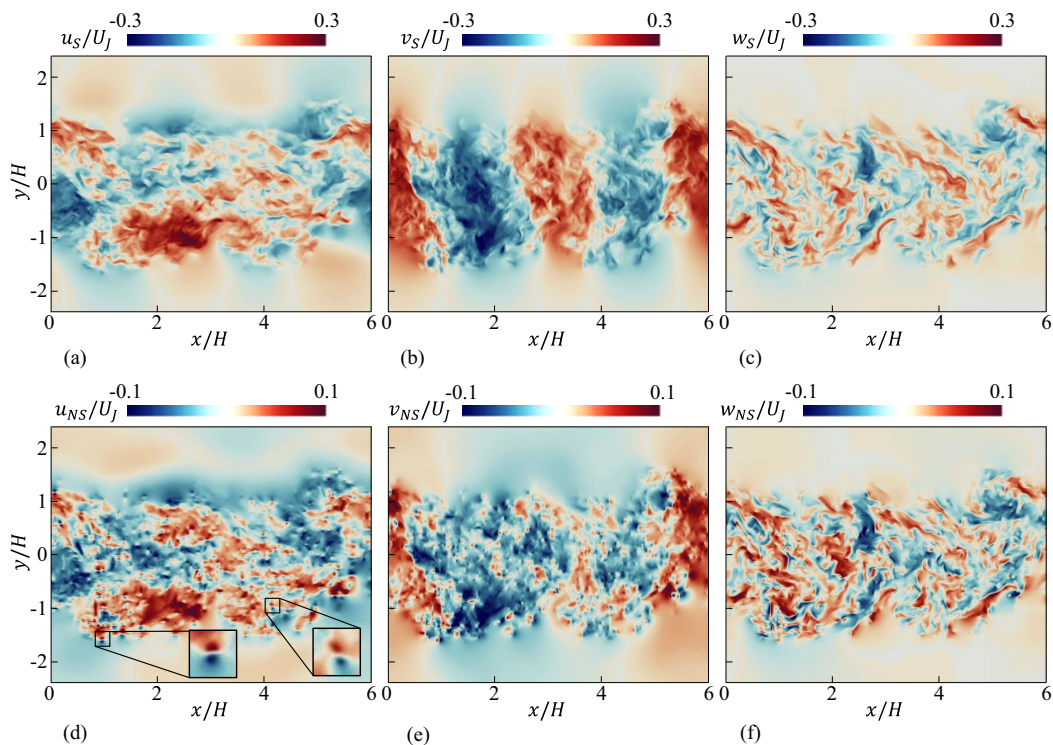
FIG. 3. Two-dimensional profiles of (a)–(c) shear and (d)–(f) nonshear components of velocity vectors on a y-z plane in the planar jet (JET2): (a), (d) streamwise velocity, (b), (e) transverse velocity, and (c), (f) spanwise velocity.

where the last two terms represent the transfer of shear and nonshear components of momentum by nonshear and shear velocities, respectively. For the normal component, the last two terms are identical. Therefore, for $i = j = x$, the decomposition is expressed as $\langle u'^2 \rangle = \langle u_S^2 \rangle + \langle u_{NS}^2 \rangle + 2\langle u_S u_{NS} \rangle$. The relative contributions to the Reynolds stress from the three terms can be evaluated by normalizing $\langle u_S^2 \rangle$, $\langle u_{NS}^2 \rangle$, and $2\langle u_S u_{NS} \rangle$ by $\langle u'^2 \rangle$. Figure 4(a) plots the normalized values of these terms as functions of the turbulent Reynolds number Re_λ for the isotropic turbulence and planar jets. The results for the jets are taken from the center ($y = 0$). Although the turbulent jet is not isotropic, the results for $\langle v'^2 \rangle$ and $\langle w'^2 \rangle$ are similar to those of $\langle u'^2 \rangle$. Therefore, the decomposition is discussed only for $\langle u'^2 \rangle$ in Fig. 4(a). The results suggest that the relative contributions of each term to $\langle u'^2 \rangle$ hardly depend on the Reynolds number and the flows. The momentum transfer due to shear, $\langle u_S^2 \rangle$, has the largest contribution to $\langle u'^2 \rangle$, and accounts for about 50% of $\langle u'^2 \rangle$. The nonshear velocity accounts only for about 10% of $\langle u'^2 \rangle$. However, the interaction of shear and nonshear velocities accounts for about 40%. Therefore, shearing motions are essential in producing the Reynolds stress in turbulence. The discussion for the off-diagonal components of $\langle u'_i u'_j \rangle$ with $i \neq j$ is given below in the context of the turbulent kinetic energy budget in the planar jet because isotropic turbulence has $\langle u'_i u'_j \rangle = 0$ with $i \neq j$. These results are also related to r.m.s. values of velocity fluctuations $u_{rms} = \sqrt{\langle u'^2 \rangle}$ although u_{rms} cannot be decomposed into three terms, unlike the normal Reynolds stress. The r.m.s. values of shear and nonshear velocities, $\sqrt{\langle u_S^2 \rangle}$ and $\sqrt{\langle u_{NS}^2 \rangle}$, are about 70% and 30% of u_{rms}, respectively. Thus, shear layers have a greater contribution to velocity fluctuations than vortex tubes.

The lateral distribution of the decomposed terms of $\langle u'^2 \rangle$ is examined for the planar jet in Fig. 4(b). The three terms of $\langle u'^2 \rangle$ are normalized by the mean velocity at the jet center, $\langle u \rangle_C$,
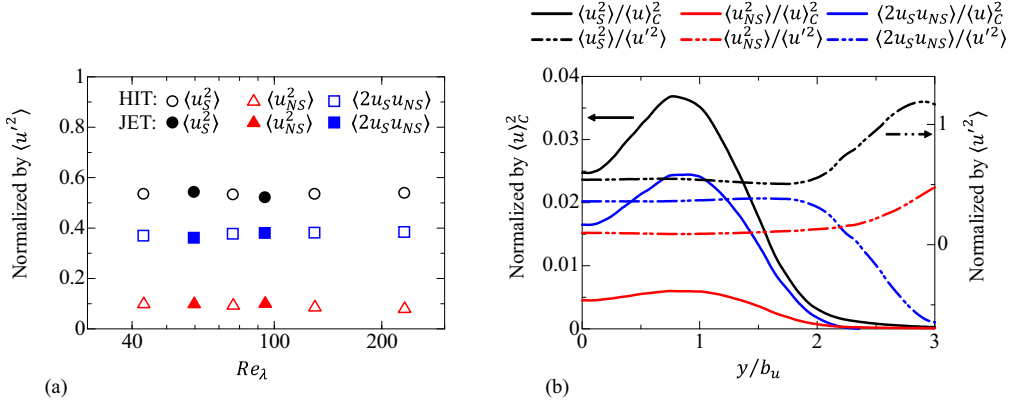
FIG. 4. (a) Re_λ dependence of a normal component of the Reynolds stress tensor decomposed by the triple decomposition as $\langle u'^2 \rangle = \langle u_S^2 \rangle + \langle u_{NS}^2 \rangle + \langle 2u_S u_{NS} \rangle$. The decomposed terms normalized by $\langle u'^2 \rangle$ are plotted as functions of Re_λ for HIT and JET. Results for JET are obtained at the center of the planar jet ($y = 0$). (b) Lateral distributions of $\langle u_S^2 \rangle$, $\langle u_{NS}^2 \rangle$, and $\langle 2u_S u_{NS} \rangle$ across the planar jet with $Re_J = 4000$. Decomposed components are normalized by the mean velocity at the center of the jet, $\langle u_C \rangle$, or the local velocity variance, $\langle u'^2 \rangle$.

or the local velocity variance $\langle u'^2 \rangle$ at each y location. The lateral position y is normalized by the jet half-width b_u defined with the mean velocity profile and is shown for $y \geqslant 0$ because the flow is statistically symmetric with respect to $y = 0$. The turbulent planar jet has a large mean velocity gradient off the centerline and the production of turbulent kinetic energy actively occurs at $y/b_u \approx 0.7$ [57]. Consistently, the velocity fluctuations are large at this location, where $\langle u_S^2 \rangle / \langle u \rangle_C^2$, $\langle u_{NS}^2 \rangle / \langle u \rangle_C^2$, and $\langle 2u_S u_{NS} \rangle / \langle u \rangle_C^2$ attain their maxima. The turbulent jet is intermittent in the sense that both turbulent and nonturbulent (ambient) fluids are observed at a fixed position. Experiments and numerical simulations have confirmed that $y/b_u \lesssim 1.0$ and $y/b_u \gtrsim 2.5$ are always in the turbulent and nonturbulent regions, respectively, while both fluids intermittently appear for $1.0 \lesssim y/b_u \lesssim 2.5$ [58,59]. Therefore, $\langle u_S^2 \rangle$, $\langle u_{NS}^2 \rangle$, and $\langle 2u_S u_{NS} \rangle$ decrease from $y/b_u \approx 1.0$ as y/b_u increases. However, these decomposed terms normalized by $\langle u'^2 \rangle$ are nearly constant up to $y/b_u \approx 1.8$. Thus, the relative contributions of shear and nonshear velocities to the Reynolds stress hardly differ in the turbulent and intermittent regions. However, $\langle u_S^2 \rangle / \langle u'^2 \rangle$ and $\langle u_{NS}^2 \rangle / \langle u'^2 \rangle$ increase with y outside the jet with $y/b_u \gtrsim 2$ while $\langle 2u_S u_{NS} \rangle$ decreases to negative values. The correlation of shear and nonshear velocities is different between the turbulent and nonturbulent regions.

Large-scale intermittency of turbulent flows is often evaluated with skewness and flatness of velocity, which are defined as $S(u') = \langle u'^3 \rangle / \langle u'^2 \rangle^{3/2}$ and $F(u') = \langle u'^4 \rangle / \langle u'^2 \rangle^2$, respectively. Figure 5(a) shows the Re_λ dependence of the skewness and flatness of u, u_S, and u_{NS}, in the isotropic turbulence and the center of the planar jet. When a variable has a probability density function described by a Gaussian function, S and F take values of 0 and 3, respectively. When large-scale motions are highly intermittent, the flatness becomes larger than 3 and the skewness often deviates from 0 [60,61]. The deviations from the Gaussian values are not large for both skewness and flatness regardless of the flows and Re_λ. Figure 5(b) shows the lateral profiles of $S(u_S)$, $S(u_{NS})$, $F(u_S)$, and $F(u_{NS})$ in the planar jet with $Re_J = 4000$. The jet core region of $y/b_u \lesssim 1$ has $S \approx 0$ and $F \approx 3$ while S and F increase in the intermittent region. The increase of S and F is explained by the intermittency of the turbulent jet because turbulent fluid with large velocity fluctuations and nonturbulent fluid with small velocity fluctuations are observed for $1.0 \lesssim y/b_u \lesssim 2.5$ [62]. Thus, the large-scale intermittency of shear and nonshear velocities is negligible for the isotropic turbulence and planar jets except for the intermittent region of the jets.

Universal relations have been observed for the Re_λ dependence of the skewness and flatness of a longitudinal velocity derivative, $S(\partial u'/\partial x)$ and $F(\partial u'/\partial x)$, in turbulent flows [2]. These relations are

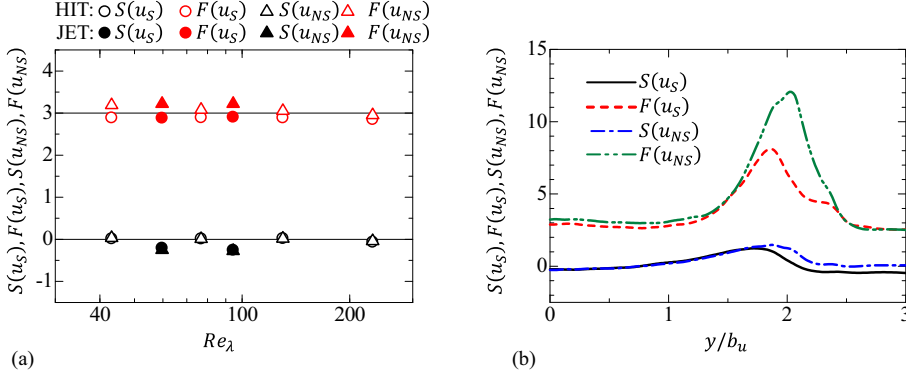FIG. 5. (a) Re_λ dependence of the skewness S and flatness F of shear (u_S) and nonshear (u_{NS}) velocity components. Results for the planar jets are obtained at the jet center ($y = 0$). (b) Lateral distributions of the skewness and flatness across the planar jet with $\mathrm{Re}_J = 4000$.

examined for the shear and nonshear velocity components. Figure 6 compares the skewness of the derivative of shear and nonshear velocities, $S(\partial u_S/\partial x)$ and $S(\partial u_{NS}/\partial x)$, with $S(\partial u'/\partial x)$ in various incompressible turbulent flows. For the range of Re_λ shown in the figure, $S(\partial u'/\partial x)$ hardly depends on Re_λ, and the present results for $S(\partial u'/\partial x)$ agree well with previous studies. For the decomposed velocity components, $S(\partial u_S/\partial x)$ is close to $S(\partial u'/\partial x)$ while $S(\partial u_{NS}/\partial x)$ is smaller in magnitude than $S(\partial u'/\partial x)$. Therefore, the universal relation between $S(\partial u'/\partial x)$ and Re_λ is attributed to the statistical properties of shearing motion. In addition, $-S(\partial u'/\partial x)$ is proportional to the production rate of enstrophy due to vortex stretching [3]. The smaller absolute values of $S(\partial u_{NS}/\partial x)$ than $S(\partial u'/\partial x)$ and $S(\partial u_S/\partial x)$ also imply that the enstrophy production in turbulence is dominated by shearing motion. This is consistent with previous studies of small-scale shear layers [12,35,67]. Figure 7 shows the Re_λ dependence of the flatness factors, $F(\partial u_S/\partial x)$ and $F(\partial u_{NS}/\partial x)$, which are compared with $F(\partial u'/\partial x)$ in various turbulent flows. An increase of $F(\partial u'/\partial x)$ with Re_λ has been reported in previous studies. Similarly, $F(\partial u_S/\partial x)$ and $F(\partial u_{NS}/\partial x)$ also increase with Re_λ. The flatness of the velocity derivative is a measure of small-scale intermittency. The flatness is similar for $\partial u_S/\partial x$ and $\partial u_{NS}/\partial x$, suggesting that both shear and nonshear velocities exhibit a similar degree of small-scale intermittency.
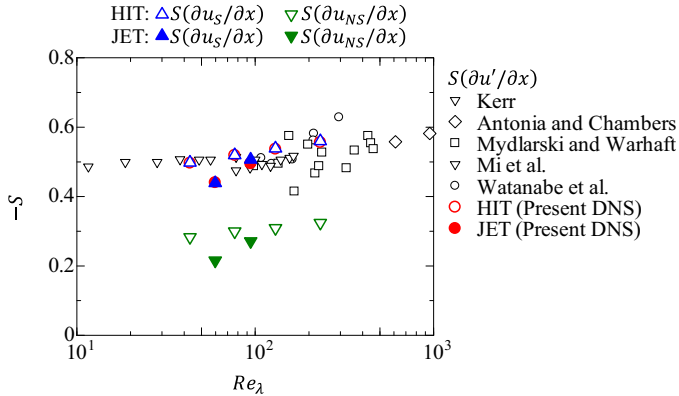

FIG. 6. Re_λ dependence of the skewness of velocity derivatives, $\partial u'/\partial x$, $\partial u_S/\partial x$, and $\partial u_{NS}/\partial x$. The results for the planar jets are obtained at the jet center ($y = 0$). The present DNS results for HIT and JET are compared with the skewness of $\partial u'/\partial x$ in other incompressible turbulent flows [39,63–66].
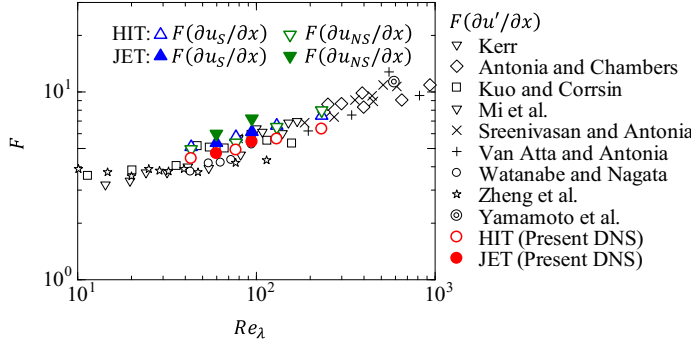
FIG. 7. Re_λ dependence of the flatness F of velocity derivatives, $\partial u'/\partial x$, $\partial u_S/\partial x$, and $\partial u_{NS}/\partial x$. The results for the planar jets are obtained at the jet center ($y = 0$). The present DNS results for HIT and JET are compared with the flatness of $\partial u'/\partial x$ in other incompressible turbulent flows [38,40,63–65,68–70].

The scale dependence of $\boldsymbol{u}_S$ and $\boldsymbol{u}_{NS}$ is examined with spectra and cospectra defined with the Fourier transform, which is applied in the x direction. The longitudinal energy spectra of u, u_S, and u_{NS} are denoted by E_u, E_{u_S}, and $E_{u_{NS}}$, respectively. Figure 8 shows E_u, E_{u_S}, and $E_{u_{NS}}$ calculated in the isotropic turbulence and at the center of the planar jets. The spectra are normalized with ε and ν while the wave number in the x direction, k_x, is normalized with the Kolmogorov scale η. For this normalization, E_u for large k_x is known to collapse onto a single curve as long as the Reynolds number is not too small [1,70]. In addition, the inertial subrange at large Re_λ satisfies $E_u \approx C\varepsilon^{2/3}k_x^{-5/3}$, which is also shown with a thin solid line. These features are well reproduced for E_u in Fig. 8(a). Similarly, E_{u_S} and $E_{u_{NS}}$ collapse well for this normalization for $k_x\eta \gtrsim 0.1$, which is in the dissipation range dominated by viscous effects. In addition, $E_{u_S} \sim k_x^{-5/3}$ becomes noticeable as the Reynolds number increases, while $E_{u_{NS}}$ tends to have a shallower slope than $k_x^{-5/3}$. This is clearly observed in the compensated spectra shown in the insets, where the power laws with $k_x^{-5/3}$ appear as horizontal lines. As the Reynolds number increases, E_{u_S} and $E_{u_{NS}}$ also tend to collapse even at a smaller wave number than the dissipation range. Therefore, the fluctuations of both shear and nonshear velocities may have universal statistical properties in the inertial subrange at a high Reynolds number. Figure 9 shows the cospectrum of u_S and u_{NS}, $C_{u_S u_{NS}}$, normalized by the spectra, E_{u_S} and $E_{u_{NS}}$, as $C_{u_S u_{NS}}/(E_{u_S}E_{u_{NS}})^{1/2}$. The cospectrum is plotted against $k_x\eta$. Large positive values are observed for large scales. This result agrees with the visualization in Figs. 1 and 3, where the large-scale distribution is correlated for shear and nonshear velocities. For small scales, the normalized cospectrum rapidly decreases for $k_x\eta \gtrsim 0.3$ and becomes negative. The scale dependence of the cospectrum is similar for both flows and different Reynolds numbers when k_x is normalized by the Kolmogorov scale. Therefore, the relation between $\boldsymbol{u}_S$ and $\boldsymbol{u}_{NS}$ strongly depends on $k_x\eta$ although the $k_x\eta$ dependence is universal in these flows. Figure 9 also indicates the normalized wavelength $\lambda_x/\eta = (2\pi/k_x)/\eta$. The decrease of the normalized cospectrum occurs for $\lambda_x/\eta \lesssim 20$. This length is close to the size of small-scale turbulent structures, such as vortex tubes and shear layers, whose diameter and thickness are about 8η and 4η, respectively [12,13,71,72]. Therefore, this λ_x dependence implies that the profiles of shear and nonshear velocities around these small-scale structures are not correlated with each other. The integral of the cospectrum yields $\langle u_S u_{NS}\rangle$, which represents the momentum transfer due to the interaction between shear and nonshear velocities. Thus, this momentum transfer actively occurs for scales greater than 20η.

C. Analyses of turbulent kinetic energy budget and scalar mixing

The decomposition of the velocity vector with the triple decomposition is useful in understanding turbulent transport phenomena, some of which are more relevant to the velocity than the velocity gradient tensor. Here we show some examples of the applications of the triple decomposition
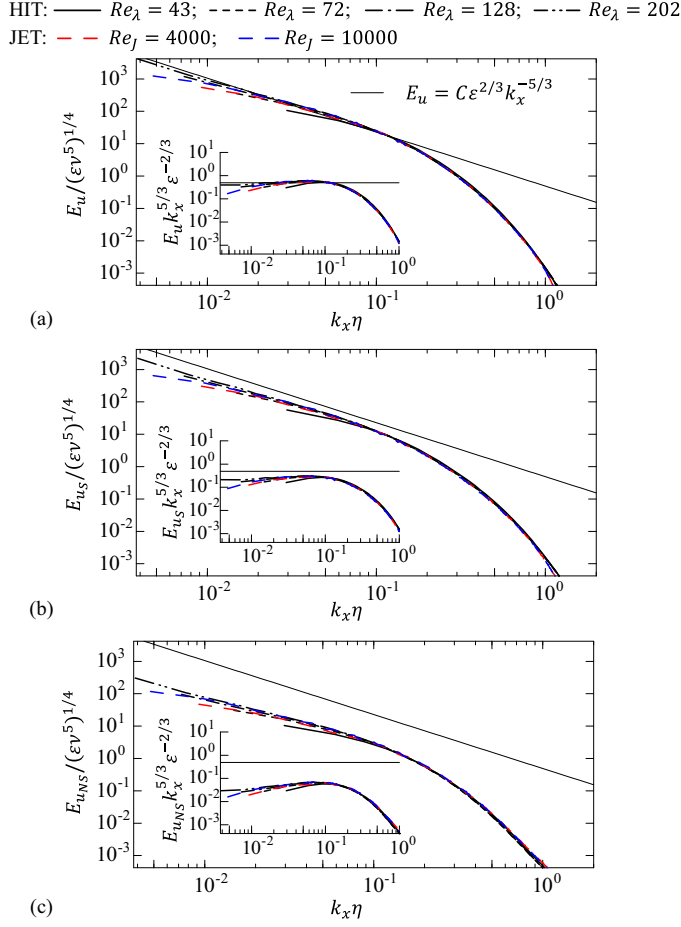
FIG. 8. One-dimensional longitudinal energy spectra in HIT and JET calculated for (a) total velocity u, E_u, (b) shear velocity u_S, E_{u_S}, and (c) nonshear velocity u_{NS}, $E_{u_{NS}}$. Results for the planar jets are obtained at the jet center ($y = 0$). The spectra and wave number k_x are nondimensionalized with the turbulent kinetic energy dissipation rate ε, kinematic viscosity ν, and Kolmogorov scale η. The spectra are also compared with $E_u = C\varepsilon^{2/3}k_x^{-5/3}$ with $C = 0.49$. Insets show the compensated spectra, $E_u k_x^{5/3}$, $E_{u_S} k_x^{5/3}$, and $E_{u_{NS}} k_x^{5/3}$, normalized by ε.

extended to the velocity field by applying the decomposition to the turbulent kinetic energy budget and turbulent mixing of a passive scalar.

The turbulent kinetic energy $k_T = \langle u_i' u_i' \rangle / 2$ is governed by the following equation [73]:

$$\frac{\partial k_T}{\partial t} + \langle u_j \rangle \frac{\partial k_T}{\partial x_j} = D_T + D_P + D_\nu + P + \varepsilon_k \tag{11}$$

with

$$D_T = -\frac{1}{2}\frac{\partial \langle u_j' u_j' u_i' \rangle}{\partial x_i}, \quad D_P = -\frac{\partial \langle u_j' p \rangle}{\partial x_j}, \quad D_\nu = \nu \frac{\partial^2 k_T}{\partial x_j \partial x_j}, \tag{12}$$

$$P = -\langle u_i' u_j' \rangle \frac{\partial \langle u_i \rangle}{\partial x_j}, \quad \varepsilon_k = -\nu \left\langle \frac{\partial u_i'}{\partial x_j} \frac{\partial u_i'}{\partial x_j} \right\rangle. \tag{13}$$
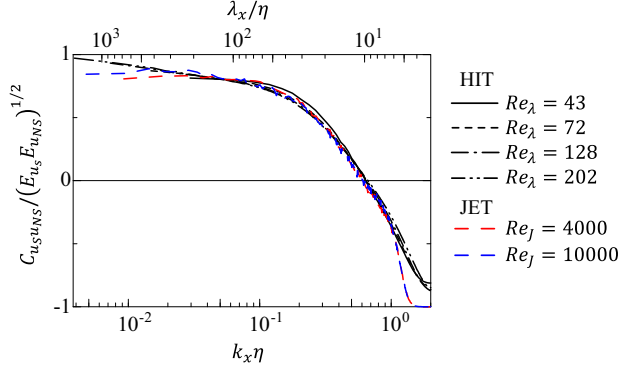
FIG. 9. Cospectrum of u_S and u_{NS}, $C_{u_S u_{NS}}$, divided by $(E_{u_S} E_{u_{NS}})^{1/2}$, where E_{u_S} and $E_{u_{NS}}$ are the longitudinal energy spectra of u_S and u_{NS}, respectively. Results for JET are obtained at the center of the planar jets ($y = 0$). The cospectrum is plotted against the wave number k_x normalized by the Kolmogorov scale η, while the corresponding wavelength $\lambda_x = 2\pi/k_x$ is also shown for reference.

Here D_T is the turbulent diffusion term, D_P is the pressure diffusion term, D_ν is the viscous diffusion term, P is the production term, and ε_k is the dissipation term. In the turbulent planar jet, D_ν is negligible except for very small Re_J. Therefore, the other terms are evaluated with the present DNS database. The triple decomposition can decompose these terms as

$$D_T = -\frac{1}{2}\frac{\partial \langle u'_j u'_j u_{S_i}\rangle}{\partial x_i} - \frac{1}{2}\frac{\partial \langle u'_j u'_j u_{NS_i}\rangle}{\partial x_i}, \tag{14}$$

$$D_P = -\frac{\partial \langle u_{S_j} p\rangle}{\partial x_j} - \frac{\partial \langle u_{NS_j} p\rangle}{\partial x_j}, \tag{15}$$

$$P = -\langle u_{S_i} u_{S_j}\rangle \frac{\partial \langle u_i\rangle}{\partial x_j} - \langle u_{NS_i} u_{NS_j}\rangle \frac{\partial \langle u_i\rangle}{\partial x_j} - [\langle u_{S_i} u_{NS_j}\rangle + \langle u_{NS_i} u_{S_j}\rangle]\frac{\partial \langle u_i\rangle}{\partial x_j}, \tag{16}$$

$$\varepsilon_k = -\nu\left\langle \frac{\partial u_{S_i}}{\partial x_j}\frac{\partial u_{S_i}}{\partial x_j}\right\rangle - \nu\left\langle \frac{\partial u_{NS_i}}{\partial x_j}\frac{\partial u_{NS_i}}{\partial x_j}\right\rangle - F_{u_S u_{NS}}. \tag{17}$$

The decomposition of D_T considers the turbulent transport of turbulent kinetic energy, $u_i u_i/2$, by the shear and nonshear velocities. Therefore, the decomposition is not applied to $u_i u_i$. For the dissipation rate, $F_{u_S u_{NS}}$ can be expressed with the correlation between $\partial u_{S_i}/\partial x_j$ and $\partial u_{NS_i}/\partial x_j$. This term is evaluated by subtracting the first and second terms from ε_k. The first and second terms of Eqs. (14)–(17) arise solely from shear and nonshear velocity components, respectively, while the third terms in Eqs. (16) and (17) are defined with their correlations. Therefore, these terms are respectively denoted by "shear," "nonshear," and "correlation." Figure 10 shows the lateral distributions of these terms in the planar jet at $\mathrm{Re}_J = 4000$. The distributions of P, ε_k, D_T, and D_P are consistent with experimental and numerical simulations of planar jets [57,74,75]. For all terms, the shear components have dominant contributions. For the production and dissipation in Figs. 10(a) and 10(b), the shear components account for about 50% of the total values. In addition, the correlation term also has a large contribution to the production term. Therefore, the nonshear velocity can produce turbulent kinetic energy mostly by the interaction with shearing motion. This is explained by the dominant contribution of $\langle u_S v_S\rangle$ and $\langle u_S v_{NS}\rangle + \langle u_{NS} v_S\rangle$ to the Reynolds stress $\langle u'v'\rangle$, and the momentum transport by shearing motions and the interactions of shear and nonshear velocities is important in the turbulent jet. The importance of shearing motion (vortex sheet) in the energy production was also pointed out in Pirozzoli *et al.* [35] although the interaction between shear and other motions was not discussed. The nonshear component has the second largest contribution to the dissipation term. The gradient of the nonshear component $\boldsymbol{u}_{NS}$ is related to both rigid-body
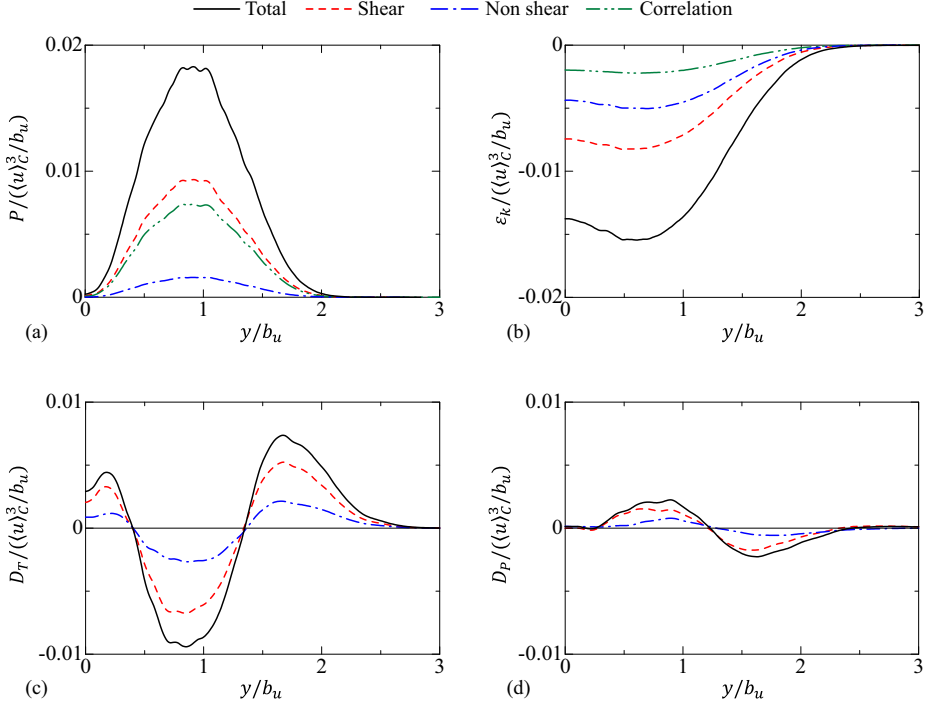
FIG. 10. Turbulent kinetic energy budget in the planar jet with $Re_J = 4000$: (a) production term P, (b) dissipation term ε_k, (c) turbulent diffusion term D_T, and (d) pressure diffusion term D_P.

rotation ∇u_R and irrotational strain ∇u_E, and the large dissipation due to the nonshear component is attributed to ∇u_E. This influence of the irrotational strain in the kinetic energy dissipation was also reported for isotropic turbulence [11]. The role of the three motions of the triple decomposition becomes clear when the viscous terms are rewritten in a different form as

$$D_v + \varepsilon_k = \left\langle \frac{\nu}{2} \frac{\partial^2 u_i' u_i'}{\partial x_j \partial x_j} \right\rangle - \nu \left\langle \frac{\partial u_i'}{\partial x_j} \frac{\partial u_i'}{\partial x_j} \right\rangle = \underbrace{\frac{\partial \langle 2\nu u_i s_{ij}' \rangle}{\partial x_j}}_{D_v'} - \underbrace{\langle 2\nu s_{ij}' s_{ij}' \rangle}_{\varepsilon_v'}, \tag{18}$$

which is derived with the following relation for the fluctuating strain-rate tensor $s_{ij}' = (\partial u_i'/\partial x_j + \partial u_j'/\partial x_i)/2$:

$$2 s_{ij}' s_{ij}' = \frac{1}{2} \left(\frac{\partial u_i'}{\partial x_j} + \frac{\partial u_j'}{\partial x_i} \right)^2 = \frac{\partial u_i'}{\partial x_j} \frac{\partial u_i'}{\partial x_j} + \frac{\partial u_i'}{\partial x_j} \frac{\partial u_j'}{\partial x_i} = \frac{\partial u_i'}{\partial x_j} \frac{\partial u_i'}{\partial x_j} + \frac{\partial}{\partial x_j} \left(u_i' \frac{\partial u_j'}{\partial x_i} \right). \tag{19}$$

These expressions for the diffusion and dissipation terms (D_v' and ε_v') are widely used in the existing literature [1,3]. The triple decomposition splits s_{ij}' into the shear and nonshear components as $s_{ij}' = (s_S')_{ij} + (s_{NS}')_{ij}$ with

$$(s_S')_{ij} = \frac{1}{2} \left(\frac{\partial u_{S_i}}{\partial x_j} + \frac{\partial u_{S_j}}{\partial x_i} \right), \quad (s_{NS}')_{ij} = \frac{1}{2} \left(\frac{\partial u_{NS_i}}{\partial x_j} + \frac{\partial u_{NS_j}}{\partial x_i} \right). \tag{20}$$

Here $\partial u_{NS_i}/\partial x_j$ corresponds to the residual tensor $(\nabla u_{RES})_{ij}$ in Eq. (2), and the symmetric part of $\partial u_{NS_i}/\partial x_j$, $(s_{NS}')_{ij}$, corresponds to elongation $(\nabla u_{EL})_{ij}$. Therefore, an instantaneous dissipation rate of turbulent kinetic energy, $2\nu s_{ij}' s_{ij}'$, can be expressed with the velocity gradient tensors of
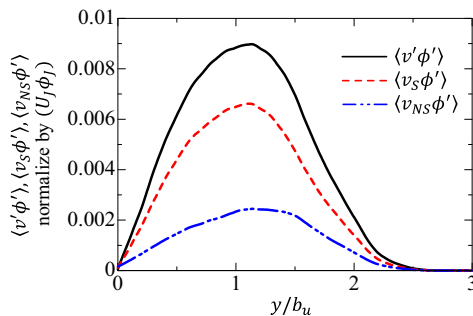
FIG. 11. Lateral distributions of the transverse turbulent flux of passive scalar, $\langle v'\phi'\rangle$, in the planar jet with $\text{Re}_J = 4000$. The flux is decomposed by the triple decomposition into the contributions from shear and nonshear velocities.

shear and elongation. For the diffusion terms in Figs. 10(c) and 10(d), the distribution is similar for both shear and nonshear components. The turbulent diffusion D_T transfers the energy from the regions with a large production rate toward the center and outside of the jet, while the pressure diffusion transfers the energy toward the center. These energy transfers are caused by both shear and nonshear velocity components although the shear component is dominant in the spatial transport of the turbulent kinetic energy.

Turbulent mixing of a passive scalar is often studied with a turbulent scalar flux $\langle u_i'\phi'\rangle$, which appears in the transport equation for the mean scalar $\langle\phi\rangle$. The triple decomposition for the velocity vector can be applied to the scalar flux as $\langle u_i'\phi'\rangle = \langle u_{S_i}\phi'\rangle + \langle u_{NS_i}\phi'\rangle$. The mean scalar transfer in the planar jet is dominated by the transverse component, $\langle v'\phi'\rangle = \langle v_S\phi'\rangle + \langle v_{NS}\phi'\rangle$. Figure 11 shows $\langle v'\phi'\rangle$, $\langle v_S\phi'\rangle$, and $\langle v_{NS}\phi'\rangle$ in the planar jet with $\text{Re}_J = 4000$. Positive values of the flux indicate the outward transfer of ϕ. Although both $\langle v_S\phi'\rangle$ and $\langle v_{NS}\phi'\rangle$ have peaks at $y/b_u \approx 1$, the peak values of $\langle v_S\phi'\rangle$ and $\langle v_{NS}\phi'\rangle$ are about 73% and 27% of the peak of $\langle v\phi'\rangle$, respectively. Therefore, the shear component has a dominant contribution to the turbulent scalar transfer.

The decomposition can also be applied to the analysis of the scale-by-scale energy budget. One of the important applications for this analysis is the interscale energy flux, which is useful to investigate the energy cascade in turbulence. In physical space, the scale dependence of turbulence is often studied with a low-pass filter [76]. The present study adapts the filter defined with a spherical average [77]:

$$\overline{f}(\boldsymbol{x}, t, r) = \frac{1}{V} \iiint G(\boldsymbol{x}, \boldsymbol{x}', r) f(\boldsymbol{x}', t) \, d\boldsymbol{x}', \tag{21}$$

with a filter function G, which is equal to 1 for $|\boldsymbol{x} - \boldsymbol{x}'| \leqslant r$ and 0 for $|\boldsymbol{x} - \boldsymbol{x}'| > r$. Equation (21) represents a volume average in a sphere with radius r centered at a point $\boldsymbol{x}$, which has a volume of $V(r) = 4\pi r^3/3$. The spherical volume average works as an isotropic top-hat filter with a cutoff length of $\Lambda = 2r$. Therefore, $\overline{f}$ contains a large-scale component of f with scales greater than Λ while a small-scale component is given by $f - \overline{f}$. The kinetic energy of fluid motion with scales smaller than Λ is represented as $k_r(\boldsymbol{x}, t, r) = \overline{u_i u_i}/2 - \overline{u_i}\,\overline{u_i}/2$, which is also called a subgrid scale kinetic energy in the context of large eddy simulation. The governing equation of k_r, which is derived for the subgrid-scale kinetic energy in LES [78,79], contains the interscale energy flux Π written as

$$\Pi = -(\overline{u_i u_j} - \overline{u_i}\,\overline{u_j})\frac{\overline{\partial u_i}}{\partial x_j}, \tag{22}$$

which represents the transfer rate of kinetic energy from fluid motion with scales greater than Λ to that with smaller scales. This term consists of the large-scale velocity gradient tensor $\overline{\partial u_i/\partial x_j}$ and
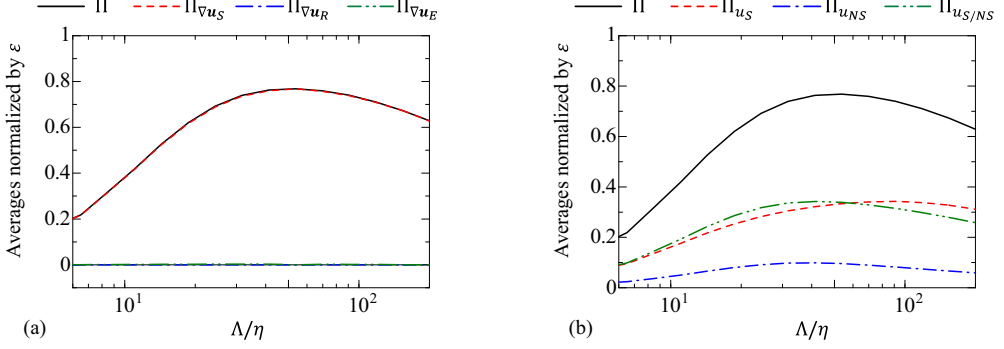
FIG. 12. Averages of the interscale kinetic energy flux $\Pi = -(\overline{u_i u_j} - \overline{u_i}\,\overline{u_j})\overline{\partial u_i/\partial x_j}$, which is decomposed into the contributions of different motions by the triple decomposition in HIT4. Decomposition is applied to (a) the large-scale velocity gradient tensor $\overline{\partial u_i/\partial x_j}$ and (b) the small-scale stress tensor $\overline{u_i u_j} - \overline{u_i}\,\overline{u_j}$.

small-scale stress tensor $\tau_{ij} = (\overline{u_i u_j} - \overline{u_i}\,\overline{u_j})$. For the triple decomposition of the velocity gradient tensor, the energy flux can be rewritten as

$$\Pi = -\tau_{ij}\overline{(\nabla\boldsymbol{u}_S)_{ij}} - \tau_{ij}\overline{(\nabla\boldsymbol{u}_R)_{ij}} - \tau_{ij}\overline{(\nabla\boldsymbol{u}_E)_{ij}} = \Pi_{\nabla\boldsymbol{u}_S} + \Pi_{\nabla\boldsymbol{u}_R} + \Pi_{\nabla\boldsymbol{u}_E}. \tag{23}$$

The triple decomposition extended for the velocity vector can also be applied for τ_{ij} to examine the role of shear and nonshear velocity components at small scales as

$$\Pi = -\tau_{S_{ij}}\overline{(\nabla\boldsymbol{u})_{ij}} - \tau_{NS_{ij}}\overline{(\nabla\boldsymbol{u})_{ij}} - \tau_{S/NS_{ij}}\overline{(\nabla\boldsymbol{u})_{ij}} = \Pi_{u_S} + \Pi_{u_{NS}} + \Pi_{u_{S/NS}}. \tag{24}$$

with $\tau_{S_{ij}} = (\overline{u_{S_i} u_{S_j}} - \overline{u_{S_i}}\,\overline{u_{S_j}})$, $\tau_{NS_{ij}} = (\overline{u_{NS_i} u_{NS_j}} - \overline{u_{NS_i}}\,\overline{u_{NS_j}})$, and $\tau_{S/NS_{ij}} = \tau_{ij} - \tau_{S_{ij}} - \tau_{NS_{ij}}$, which, respectively, represent the small-scale stresses due to the shear velocity, the nonshear velocity, and their interaction.

The averages of Π and its decomposed terms are calculated with a wide range of the cutoff length Λ. Figure 12 shows the scale dependence of $\langle\Pi\rangle$, $\langle\Pi_{\nabla\boldsymbol{u}_S}\rangle$, $\langle\Pi_{\nabla\boldsymbol{u}_R}\rangle$, and $\langle\Pi_{\nabla\boldsymbol{u}_E}\rangle$ in HIT4. Positive $\langle\Pi\rangle$ indicates that the kinetic energy is transferred from large to small scales. The present results with $\langle\Pi\rangle \approx \langle\Pi_{\nabla\boldsymbol{u}_S}\rangle$, $\langle\Pi_{\nabla\boldsymbol{u}_R}\rangle \approx 0$, and $\langle\Pi_{\nabla\boldsymbol{u}_E}\rangle \approx 0$ indicate that this interscale energy transfer is mainly caused by the interaction between the small-scale stress and large-scale velocity gradient arising from shearing motion while the large-scale velocity gradients for motions of rigid-body rotation and elongation have negligible contributions.

Figure 12(b) presents $\langle\Pi\rangle$, $\langle\Pi_{u_S}\rangle$, $\langle\Pi_{u_{NS}}\rangle$, and $\langle\Pi_{u_{S/NS}}\rangle$ in HIT4. The small-scale stress due to the nonshear velocity component only weakly contributes to $\langle\Pi\rangle$, as attested by the smallest $\langle\Pi_{u_{NS}}\rangle$ among the three decomposed terms. Both shear and correlation terms, $\langle\Pi_{u_S}\rangle$ and $\langle\Pi_{u_{S/NS}}\rangle$, are equally important in the interscale energy transfer.

The decomposition of both τ_{ij} and $\overline{\partial u_i/\partial x_j}$ leads to the following decomposition of Π:

$$\Pi = \underbrace{-\tau_{S_{ij}}\overline{(\nabla\boldsymbol{u}_S)_{ij}}}_{\Pi_{u_S}^S} \underbrace{-\tau_{NS_{ij}}\overline{(\nabla\boldsymbol{u}_S)_{ij}}}_{\Pi_{u_{NS}}^S} \underbrace{-\tau_{S/NS_{ij}}\overline{(\nabla\boldsymbol{u}_S)_{ij}}}_{\Pi_{u_{S/NS}}^S}$$

$$\underbrace{-\tau_{S_{ij}}\overline{(\nabla\boldsymbol{u}_R)_{ij}}}_{\Pi_{u_S}^R} \underbrace{-\tau_{NS_{ij}}\overline{(\nabla\boldsymbol{u}_R)_{ij}}}_{\Pi_{u_{NS}}^R} \underbrace{-\tau_{S/NS_{ij}}\overline{(\nabla\boldsymbol{u}_R)_{ij}}}_{\Pi_{u_{S/NS}}^R}$$

$$\underbrace{-\tau_{S_{ij}}\overline{(\nabla\boldsymbol{u}_E)_{ij}}}_{\Pi_{u_S}^E} \underbrace{-\tau_{NS_{ij}}\overline{(\nabla\boldsymbol{u}_E)_{ij}}}_{\Pi_{u_{NS}}^E} \underbrace{-\tau_{S/NS_{ij}}\overline{(\nabla\boldsymbol{u}_E)_{ij}}}_{\Pi_{u_{S/NS}}^E}. \tag{25}$$
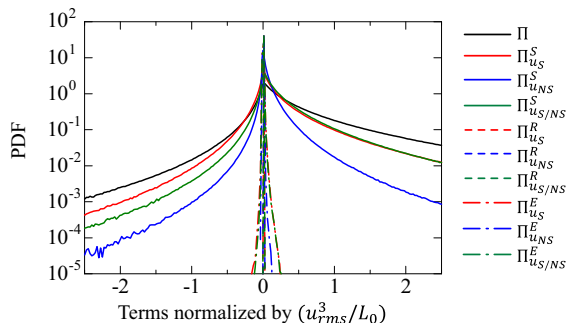
FIG. 13. Probability density functions (PDFs) of the interscale kinetic energy flux $\Pi = -(\overline{u_i u_j} - \overline{u_i}\,\overline{u_j})(\overline{\partial u_i / \partial x_j})$ at $\Lambda/\eta = 18$ in HIT4. The PDF is shown for the terms decomposed by the triple decomposition in Eq. (25).

Here the subscript and superscript of $\Pi^\beta_{u_\alpha}$ represent the decompositions of τ_{ij} and $\overline{\partial u_i / \partial x_j}$, respectively. Figure 13 shows the PDF of Π and $\Pi^\beta_{u_\alpha}$ at $\Lambda/\eta = 18$. For the terms related to the velocity gradients of rigid-body rotation and elongation, $\Pi^R_{u_\alpha}$ and $\Pi^E_{u_\alpha}$ with $\alpha = S$, NS, or S/NS, the PDF has a large peak at $\Pi^R_{u_\alpha} = 0$ and $\Pi^E_{u_\alpha} = 0$. The PDF of Π and $\Pi^S_{u_\alpha}$ is positively skewed for all terms. These results indicate that the forward energy transfer from large to small scales is dominant for the large-scale velocity gradient of shearing motion. In contrast, the large-scale velocity gradients of rigid-body rotation and elongation hardly contribute to the interscale energy transfer. Here $\Pi^S_{u_S}$ and $\Pi^S_{u_{S/NS}}$ tend to be larger than the other terms. The interscale energy transfer is caused by the interplay of the large-scale velocity gradient of shearing motion with the small-scale stresses arising from the shear velocity or the interaction between shear and nonshear velocities. The inverse transfer from small to large scales with negative values of the fluxes occurs less frequently for $\Pi^S_{u_{S/NS}}$ than for $\Pi^S_{u_S}$. Therefore, the mean flux at $\Lambda/\eta = 18$ in Fig. 12(b) is the largest for the small-scale stress arising from the interaction between the shear and nonshear velocity components. These statistics for the decomposed energy flux show that shearing motion plays an important role in the energy cascade process in turbulence.

V. CONCLUSION

The triple decomposition of a velocity gradient tensor has been extended for the decomposition of a velocity field. The present approach adapts the Biot-Savart law to reconstruct shear and nonshear velocities from the vorticity vectors of shear and rigid-body rotation, respectively. The characteristics of shear and nonshear velocities have been investigated with DNS databases of homogeneous isotropic turbulence and temporally evolving planar jets. These decomposed velocities are related to the flow arising from the superposition of many shear layers or vortex tubes. Therefore, the present decomposition provides an interesting framework to study the flows induced by these small-scale structures in turbulence, which will be useful in understanding their roles in turbulent transport phenomena, as discussed in this study.

Statistical properties of shear and nonshear velocities have been compared for isotropic turbulence and planar jets to examine their dependence on the flows and Reynolds numbers. Both shear and nonshear velocities are contributed to by fluid motion with a wide range of length scales. The r.m.s. values of shear and nonshear velocities are about 70% and 30% of the r.m.s. value of total velocity fluctuations, respectively, and shear layers have a greater contribution to velocity fluctuations than vortex tubes. The decomposition applied to the Reynolds stress suggests that the momentum transport is dominated by the self-transfer of shear velocity and the interaction between the shear and nonshear velocity components. The relative contributions of decomposed components of the Reynolds stress tensor hardly differ for both isotropic turbulence and planar jets

with different Reynolds numbers. In addition, the large-scale intermittency for shear and nonshear velocities is not significant in both turbulent flows. These universal natures concern the turbulent core region of the jet while different tendencies are observed for the intermittent region and ambient flow, where the flow is partially or fully nonturbulent (laminar). The Reynolds number dependence of the skewness of the longitudinal velocity derivative implies that the shear velocity is essential in enstrophy production. The flatness factors of the velocity derivative suggest that the small-scale intermittency is at a similar degree for shear and nonshear velocities. The energy spectra of shear and nonshear velocities in different flows and Reynolds numbers collapse well in the dissipation range ($k_x \eta \gtrsim 0.1$) when they are normalized by the Kolmogorov scales, and small-scale fluctuations tend to be statistically universal for both shear and nonshear velocities. In addition, as the Reynolds number increases, the spectra for larger scales of $k_x \eta \lesssim 0.1$ also tend to follow a single line for the isotropic turbulence and planar jets. The spectra of shear velocity also tend to obey a power law with an exponent of $-5/3$ at a high Reynolds number. The shear and nonshear velocities are positively correlated at large scales while this correlation rapidly decreases for wave numbers smaller than $k_x \eta \approx 0.3$. Thus, the momentum transfer due to the interaction between shear and nonshear velocities is the feature of large-scale turbulent motions. The present results infer that some of the statistical properties of shear and nonshear velocities are universal in the inertial range when the Reynolds number is sufficiently large. However, further investigations are also required for this issue because only two types of turbulent flows with a limited range of Re_λ are considered in the present study.

Important applications of the triple decomposition extended to velocity vectors are the analyses of turbulent transport phenomena. The present study has also presented such examples for the turbulent kinetic energy budget and passive scalar mixing. The shear velocity and its interaction with the nonshear velocity are shown to be dominant in the inviscid terms, such as energy production and turbulent and pressure diffusion. The decomposition applied to the turbulent scalar flux also confirms that the shear velocity has a larger contribution to the turbulent transport of a passive scalar in the jet than the nonshear velocity. The present study has also adapted the triple decomposition to the analysis of the energy cascade, which is quantified as the interscale energy flux defined with a low pass filter. The flux is expressed as the product of the small-scale stress and large-scale velocity gradient tensor, for which the triple decomposition is applied. The interscale energy flux is dominated by the large-scale velocity gradient due to shearing motion while those due to rigid-body rotation and elongation have negligible influences on the energy flux. The small-scale stress arising solely from the nonshear velocity also does not cause a large energy flux. The interscale energy flux is shown to be dominated by the small-scale stresses due to the shear velocity or the interaction between shear and nonshear velocities. These results suggest the importance of shearing motion in the dynamical properties of turbulent flows.

[1] S. B. Pope, *Turbulent Flows* (Cambridge University Press, Cambridge, UK, 2000).

[2] K. R. Sreenivasan and R. A. Antonia, The phenomenology of small-scale turbulence, Annu. Rev. Fluid Mech. **29**, 435 (1997).

[3] P. A. Davidson, *Turbulence: An Introduction for Scientists and Engineers* (Oxford University Press, New York, 2004).

[4] J. Jiménez, A. A. Wray, P. G. Saffman, and R. S. Rogallo, The structure of intense vorticity in isotropic turbulence, J. Fluid Mech. **255**, 65 (1993).

[5] A. Vincent and M. Meneguzzi, The dynamics of vorticity tubes in homogeneous turbulence, J. Fluid Mech. **258**, 245 (1994).

[6] M. Hayashi, T. Watanabe, and K. Nagata, The relation between shearing motions and the turbulent/non-turbulent interface in a turbulent planar jet, Phys. Fluids **33**, 055126 (2021).

[7] V. Kolář, Vortex identification: New requirements and limitations, Int. J. Heat Fluid Flow **28**, 638 (2007).

[8] C. Liu, Y. Gao, S. Tian, and X. Dong, Rortex-A new vortex vector definition and vorticity tensor and vector decompositions, Phys. Fluids **30**, 035103 (2018).

[9] Y. Maciel, M. Robitaille, and S. Rahgozar, A method for characterizing cross-sections of vortices in turbulent flows, Int. J. Heat Fluid Flow **37**, 177 (2012).

[10] J. Eisma, J. Westerweel, G. Ooms, and G. E. Elsinga, Interfaces and internal layers in a turbulent boundary layer, Phys. Fluids **27**, 055103 (2015).

[11] R. Nagata, T. Watanabe, K. Nagata, and C. B. da Silva, Triple decomposition of velocity gradient tensor in homogeneous isotropic turbulence, Comput. Fluids **198**, 104389 (2020).

[12] T. Watanabe, K. Tanaka, and K. Nagata, Characteristics of shearing motions in incompressible isotropic turbulence, Phys. Rev. Fluids **5**, 072601(R) (2020).

[13] D. Fiscaletti, O. R. H. Buxton, and A. Attili, Internal layers in turbulent free-shear flows, Phys. Rev. Fluids **6**, 034612 (2021).

[14] M. Breda and O. R. H. Buxton, Effects of multiscale geometry on the large-scale coherent structures of an axisymmetric turbulent jet, J. Vis. **21**, 525 (2018).

[15] A. Attili, J. C. Cristancho, and F. Bisetti, Statistics of the turbulent/non-turbulent interface in a spatially developing mixing layer, J. Turbul. **15**, 555 (2014).

[16] G. E. Elsinga and I. Marusic, Universal aspects of small-scale motions in turbulence, J. Fluid Mech. **662**, 514 (2010).

[17] G. E. Elsinga, T. Ishihara, M. V. Goudar, C. B. da Silva, and J. C. R. Hunt, The scaling of straining motions in homogeneous isotropic turbulence, J. Fluid Mech. **829**, 31 (2017).

[18] Y. Sakurai and T. Ishihara, Relationships between small-scale fluid motions and inertial particle clustering in turbulence, J. Phys. Soc. Jpn. **87**, 093401 (2018).

[19] G. E. Elsinga and I. Marusic, The anisotropic structure of turbulence and its energy spectrum, Phys. Fluids **28**, 011701 (2016).

[20] M. V. Goudar and G. E. Elsinga, Tracer particle dispersion around elementary flow patterns, J. Fluid Mech. **843**, 872 (2018).

[21] T. Watanabe and K. Nagata, The response of small-scale shear layers to perturbations in turbulence, J. Fluid Mech. **963**, A31 (2023).

[22] J. C. Vassilicos, Dissipation in turbulent flows, Annu. Rev. Fluid Mech. **47**, 95 (2015).

[23] K. Takamure, Y. Ito, Y. Sakai, K. Iwano, and T. Hayase, Momentum transport process in the quasi self-similar region of free shear mixing layer, Phys. Fluids **30**, 015109 (2018).

[24] M. Takahashi, K. Iwano, Y. Sakai, and Y. Ito, Three-dimensional visualization of destruction events of turbulent momentum transfer in a plane jet, Phys. Fluids **31**, 105114 (2019).

[25] T. Akao, T. Watanabe, and K. Nagata, Vertical confinement effects on a fully developed turbulent shear layer, Phys. Fluids **34**, 055129 (2022).

[26] M. Farge, K. Schneider, and N. Kevlahan, Non-Gaussianity and coherent vortex simulation for two-dimensional turbulence using an adaptive orthogonal wavelet basis, Phys. Fluids **11**, 2187 (1999).

[27] M. Farge, G. Pellegrino, and K. Schneider, Coherent Vortex Extraction in 3D Turbulent Flows Using Orthogonal Wavelets, Phys. Rev. Lett. **87**, 054501 (2001).

[28] N. Okamoto, K. Yoshimatsu, K. Schneider, M. Farge, and Y. Kaneda, Coherent vortices in high resolution direct numerical simulation of homogeneous isotropic turbulence: A wavelet viewpoint, Phys. Fluids **19**, 115109 (2007).

[29] C. Beta, K. Schneider, M. Farge, and H. Bockhorn, Numerical study of mixing of passive and reactive scalars in two-dimensional turbulent flows using orthogonal wavelet filtering, Chem. Eng. Sci. **58**, 1463 (2003).

[30] T. Watanabe, Y. Sakai, K. Nagata, Y. Ito, and T. Hayase, Wavelet analysis of coherent vorticity near the turbulent/non-turbulent interface in a turbulent planar jet, Phys. Fluids **26**, 095105 (2014).

[31] L. Biferale, G. Boffetta, A. Celani, A. Lanotte, and F. Toschi, Particle trapping in three-dimensional fully developed turbulence, Phys. Fluids **17**, 021701 (2005).

[32] T. Watanabe, R. Jaulino, R. R. Taveira, C. B. da Silva, K. Nagata, and Y. Sakai, Role of an isolated eddy near the turbulent/non-turbulent interface layer, Phys. Rev. Fluids **2**, 094607 (2017).

[33] M. M. Neamtu-Halic, J.-P. Mollicone, M. Van Reeuwijk, and M. Holzner, Role of vortical structures for enstrophy and scalar transport in flows with and without stable stratification, J. Turbul. **22**, 393 (2021).

[34] J. Kronborg and J. Hoffman, The triple decomposition of the velocity gradient tensor as a standardized real Schur form, Phys. Fluids **35**, 031703 (2023).

[35] S. Pirozzoli, M. Bernardini, and F. Grasso, On the dynamical relevance of coherent vortical structures in turbulent boundary layers, J. Fluid Mech. **648**, 325 (2010).

[36] T. Watanabe and K. Nagata, Energetics and vortex structures near small-scale shear layers in turbulence, Phys. Fluids **34**, 095114 (2022).

[37] Y. Morinishi, T. S. Lund, O. V. Vasilyev, and P. Moin, Fully conservative higher order finite difference schemes for incompressible flow, J. Comput. Phys. **143**, 90 (1998).

[38] T. Watanabe and K. Nagata, Integral invariants and decay of temporally developing grid turbulence, Phys. Fluids **30**, 105111 (2018).

[39] T. Watanabe, X. Zhang, and K. Nagata, Direct numerical simulation of incompressible turbulent boundary layers and planar jets at high Reynolds numbers initialized with implicit large eddy simulation, Comput. Fluids **194**, 104314 (2019).

[40] K. Yamamoto, T. Ishida, T. Watanabe, and K. Nagata, Experimental and numerical investigation of compressibility effects on velocity derivative flatness in turbulence, Phys. Fluids **34**, 055101 (2022).

[41] P. L. Carroll and G. Blanquart, A proposed modification to Lundgren's physical space velocity forcing method for isotropic turbulence, Phys. Fluids **25**, 105114 (2013).

[42] M. Hayashi, T. Watanabe, and K. Nagata, Characteristics of small-scale shear layers in a temporally evolving turbulent planar jet, J. Fluid Mech. **920**, A38 (2021).

[43] C. B. da Silva and J. C. F. Pereira, Invariants of the velocity-gradient, rate-of-strain, and rate-of-rotation tensors across the turbulent/nonturbulent interface in jets, Phys. Fluids **20**, 055101 (2008).

[44] M. van Reeuwijk and M. Holzner, The turbulence boundary of a temporal jet, J. Fluid Mech. **739**, 254 (2014).

[45] A. Cimarelli, A. Fregni, J.-P. Mollicone, M. Van Reeuwijk, and E. De Angelis, Structure of turbulence in temporal planar jets, Phys. Fluids **34**, 045109 (2022).

[46] M. Takahashi, R. Fukui, K. Tsujimoto, T. Ando, and T. Shakouchi, Helical structures in a temporally developing round jet in the developed state, Flow, Turbul. Combust. **111**, 59 (2023).

[47] P. J. Diamessis, G. R. Spedding, and J. A. Domaradzki, Similarity scaling and vorticity structure in high-Reynolds-number stably stratified turbulent wakes, J. Fluid Mech. **671**, 52 (2011).

[48] R. Jahanbakhshi, N. S. Vaghefi, and C. K. Madnia, Baroclinic vorticity generation near the turbulent/non-turbulent interface in a compressible shear layer, Phys. Fluids **27**, 105105 (2015).

[49] M. Kozul, D. Chung, and J. P. Monty, Direct numerical simulation of the incompressible temporally developing turbulent boundary layer, J. Fluid Mech. **796**, 437 (2016).

[50] T. Watanabe, X. Zhang, and K. Nagata, Turbulent/non-turbulent interfaces detected in DNS of incompressible turbulent boundary layers, Phys. Fluids **30**, 035102 (2018).

[51] T. Watanabe, Y. Zheng, and K. Nagata, The decay of stably stratified grid turbulence in a viscosity-affected stratified flow regime, J. Fluid Mech. **946**, A29 (2022).

[52] T. Watanabe and K. Nagata, Large-scale characteristics of a stably stratified turbulent shear layer, J. Fluid Mech. **927**, A27 (2021).

[53] I. Namer and M. V. Ötügen, Velocity measurements in a plane turbulent air jet at moderate Reynolds numbers, Exp. Fluids **6**, 387 (1988).

[54] M. Klein, A. Sadiki, and J. Janicka, Investigation of the influence of the Reynolds number on a plane jet using direct numerical simulation, Int. J. Heat Fluid Flow **24**, 785 (2003).

[55] T. Ishihara, Y. Kaneda, and J. C. R. Hunt, Thin shear layers in high Reynolds number turbulence–DNS results, Flow, Turbul. Combust. **91**, 895 (2013).

[56] S. Pirozzoli, M. Bernardini, and F. Grasso, Characterization of coherent vortical structures in a supersonic turbulent boundary layer, J. Fluid Mech. **613**, 205 (2008).

[57] O. Terashima, Y. Sakai, and K. Nagata, Simultaneous measurement of velocity and pressure in a plane jet, Exp. Fluids **53**, 1149 (2012).

[58] T. Watanabe, Y. Sakai, K. Nagata, Y. Ito, and T. Hayase, Enstrophy and passive scalar transport near the turbulent/non-turbulent interface in a turbulent planar jet flow, Phys. Fluids **26**, 105103 (2014).

[59] T. Watanabe, T. Naito, Y. Sakai, K. Nagata, and Y. Ito, Mixing and chemical reaction at high Schmidt number near turbulent/nonturbulent interface in planar liquid jet, Phys. Fluids **27**, 035114 (2015).

[60] S. Veeravalli and Z. Warhaft, The shearless turbulence mixing layer, J. Fluid Mech. **207**, 191 (1989).

[61] H. S. Kang and C. Meneveau, Experimental study of an active grid-generated shearless mixing layer and comparisons with large-eddy simulation, Phys. Fluids **20**, 125102 (2008).

[62] R. C. Deo, G. J. Nathan, and J. Mi, Similarity analysis of the momentum field of a subsonic, plane air jet with varying jet-exit and local Reynolds numbers, Phys. Fluids **25**, 015115 (2013).

[63] R. M. Kerr, Higher-order derivative correlations and the alignment of small-scale structures in isotropic numerical turbulence, J. Fluid Mech. **153**, 31 (1985).

[64] J. Mi, M. Xu, and T. Zhou, Reynolds number influence on statistical behaviors of turbulence in a circular free jet, Phys. Fluids **25**, 075101 (2013).

[65] R. A. Antonia and A. J. Chambers, On the correlation between turbulent velocity and temperature derivatives in the atmospheric surface layer, Boundary Layer Meteorol. **18**, 399 (1980).

[66] L. Mydlarski and Z. Warhaft, On the onset of high-Reynolds-number grid-generated wind tunnel turbulence, J. Fluid Mech. **320**, 331 (1996).

[67] O. R. H. Buxton and B. Ganapathisubramani, Amplification of enstrophy in the far field of an axisymmetric turbulent jet, J. Fluid Mech. **651**, 483 (2010).

[68] A. Y.-S. Kuo and S. Corrsin, Experiments on internal intermittency and fine-structure distribution functions in fully turbulent fluid, J. Fluid Mech. **50**, 285 (1971).

[69] C. W. Van Atta and R. A. Antonia, Reynolds number dependence of skewness and flatness factors of turbulent velocity derivatives, Phys. Fluids **23**, 252 (1980).

[70] Y. Zheng, K. Nagata, and T. Watanabe, Energy dissipation and enstrophy production/destruction at very low Reynolds numbers in the final stage of the transition period of decay in grid turbulence, Phys. Fluids **33**, 035147 (2021).

[71] S.-J. Kang, M. Tanahashi, and T. Miyauchi, Dynamics of fine scale eddy clusters in turbulent channel flows, J. Turbul. **8**, N52 (2007).

[72] A. A. Ghira, G. E. Elsinga, and C. B. da Silva, Characteristics of the intense vorticity structures in isotropic turbulence at high Reynolds numbers, Phys. Rev. Fluids **7**, 104605 (2022).

[73] F. T. Nieuwstadt, J. Westerweel, and B. Boersma, *Introduction to Theory and Applications of Turbulent Flows* (Springer, Cham, Switzerland, 2016).

[74] S. A. Stanley, S. Sarkar, and J. P. Mellado, A study of the flow-field evolution and mixing in a planar turbulent jet using direct numerical simulation, J. Fluid Mech. **450**, 377 (2002).

[75] T. Watanabe, Y. Sakai, K. Nagata, and Y. Ito, Large eddy simulation study of turbulent kinetic energy and scalar variance budgets and turbulent/non-turbulent interface in planar jets, Fluid Dyn. Res. **48**, 021407 (2016).

[76] J. Wang, Y. Yang, Y. Shi, Z. Xiao, X. T. He, and S. Chen, Cascade of Kinetic Energy in Three-Dimensional Compressible Turbulence, Phys. Rev. Lett. **110**, 214505 (2013).

[77] T. Watanabe, C. B. da Silva, and K. Nagata, Scale-by-scale kinetic energy budget near the turbulent/nonturbulent interface, Phys. Rev. Fluids **5**, 124610 (2020).

[78] U. Piomelli, Y. Yu, and R. J. Adrian, Subgrid-scale energy transfer and near-wall turbulence structure, Phys. Fluids **8**, 215 (1996).

[79] C. B. da Silva and O. Métais, On the influence of coherent structures upon interscale interactions in turbulent plane jets, J. Fluid Mech. **473**, 103 (2002).